Correlation of optical observations of objects in Earth orbit

J.M. Maruskin[1], D.J. Scheeres[2], and K.T. Alfriend[3]

Abstract

A sequence of optical measurements of an Earth orbiting object over one track has sufficient information to determine the angles and angular rates with some degree of precision, but cannot measure the range or range-rate. Despite the lack of complete state information, constraints on range and range-rate can be determined by applying physical constraints. Applying these constraints to an observation constrains an object's state to lie within a two-dimensional lamina in phase space. Such a region can be mapped into orbital element space and propagated in time. As the regions in question are two-dimensional lamina it is possible to model them with high precision without excessive computational burden. A second observation of a space object can similarly be mapped into a lamina in orbit element space and intersected with a previous observation mapped to the same epoch. If the object is the same, this intersection process yields a non-zero set which may be unique, depending on observational geometries. If the object is different the intersection is null in general. Addition of uncertainty in the angle and angle-rate measurements yields finite regions of intersection, sufficient to localize an initial estimate for a connecting orbit if the two mapped observation lamina have regions of non-zero intersection. If the lamina are mapped into a Hamiltonian canonical set of elements, such as the Delaunay or Hamiltonian elements, the projection of this lamina into the conjugate pairs of coordinates and momenta must sum to a constant, due to the integral invariants of Poincarè-Cartan. This provides additional structure to these regions as this integral invariance is conserved when mapping in time and thus the area of these projections remain constant.

1 Introduction

A problem of recent interest to space faring nations is the tracking, orbit determination, and cataloging of all pieces of artificial space debris particles in low, medium, and high Earth orbits, a population of more than 300,000 particles. The United States Air Force Space Command has installed a network of 25 radar and optical sensors for

---

[1] Ph.D. Candidate, Department of Mathematics, The University of Michigan, jmaruski@umich.edu

[2] Associate Professor, Department of Aerospace Engineering, The University of Michigan, scheeres@umich.edu

[3] TEES Distinguished Research Chair Professor, Texas A&M University, alfriend@aeromail.tamu.edu

this task, which make about 80,000 observations per night. For more background on observation of Space Debris, see Rossi [20, 21].

Using optical measurements for particles in medium to high Earth orbits, the angles and angular rates of the passing particles, as seen from an Earth-based telescope, can be measured to high precision, however the range and range-rates are largely undetermined. The set of angles and angular rates of such a measurement is called an *attributable vector.* Recent work has been done in outlining a precise mathematical description of the *admissible region* of the range, range-rate plane given an attributable vector observed by radar or optical measurements, Tommei et al. [25]. The admissible region is a two-dimensional surface that lives in the six-dimensional phase space surrounding the Earth. This uncertainty surface is then discretized by a number of points called *Virtual Debris particles*, or VD's. For optical measurements, the admissible region on the range range-rate plane is only restricted by the fact that the debris particle should be gravitationally bound to the Earth (negative geocentric energy) and that it lie within some region (2 and 20 Earth radii) of the observer (Tommei et al. [25]). Our preliminary numerical analysis of a randomaly chosen attributable vector and its corresponding VD field showed that before several hours had passed, about half of the VD's will have crashed into the Earth. Motivated by these observations, we present in this paper a tighter restriction on the uncertainty region of the range range-rate plane. In particular, in addition to demanding the distance between the debris particle and observer lie between 2 and 20 Earth radii, we place restrictions on the periapsis and apoapsis of the orbit. We require the orbit's periapsis to be greater than 1 Earth radius plus 200 km, and the apoapsis to be less than 25 Earth radii. This places additional constraints on the admissible region and reduces its size considerably.

In §3, we introduce Delaunay variables and discuss the transformation between the observation space (polar coordinates centered at the observation site on Earth's surface) and Delaunay space, and the corresponding State Transition Matrix (STM) of the transformation. Delaunay variables were introduced by Delaunay [8, 9], and can be derived several ways. One can derive them by solving the Hamilton-Jacobi equations (Born [3]) or by using Lagrange brackets (Brouwer & Clemence [4]; Abraham & Marsden [1]). A modern geometric derivation is given in Chang & Marsden [5]. A nice aspect of Delaunay variables is that they can be written in symplectic (canonical) coordinate-conjugate momentum pairs. The corresponding equations of motion, even for the perturbed problem, can be written in the form of Hamilton's equations. Therefore the integral invariants of Poincaré-Cartan apply, and the sum of the signed area projections onto the three symplectic planes must be conserved. The Delaunay variables are also the action-angle variables of the two body problem; the angles are the coordinates and the actions are the momenta. For the Kepler problem, all Delaunay variables except a single angle variable are conserved. Even though the two-dimensional uncertainty distribution in geocentric cartesion wraps around the Earth in phase space rapidly, the projection of the same uncertainty distribution on 2 of the 3 Delaunay planes is static. The angle variable of the third plane is the mean anomaly, so all the VD particles march at different rates (which depend only on the mean anomaly's conjugate momentum) along this direction. Since the angle variables are modulo 2π, the surface begins to wrap around and becomes more and more "shredded" as time progresses. Even in the averaged perturbed problem, only the angle variables change in time, so that the same shredding can be seen in each of the symplectic planes.

In §5 - §7 we will discuss an algorithm for correlating two observations of the same debris particle. We will first consider the case of having two zenith observations at our disposal. We will then add some fuzz to the uncertainty distribution by considering near-zenith observations. Finally we discuss the case when the J_2 term is added to Earth's potential energy. An earlier version of this paper was given in [16], the current paper is updated by a more in-depth discussion of the information content in a single track of optical data and in a discussion of the effect of uncertainty in the attributable vector on the distribution in the Delaunay planes.

2 Admissible Region

In this section we shall review the *admissible region* for a space debris particle observed by a ground based optical sensor, as presented in Tommei et al. [25], and offer an additional physical constraint that will further limit the size of this region in the range range-rate plane.

2.1 Attributable Vectors

Let P be the geocentric position of a space debris particle and P_O the geocentric position of the optical observer. Let the position of the debris particle with respect to the observer be denoted $P_D = \rho\hat{R}$, where $\hat{R}$ is a unit vector pointing from the observer to the particle. This gives us:

$$P = P_O + P_D$$

Let

$$(\rho, \alpha, \delta) \in \mathbb{R}^+ \times [-\pi, \pi) \times (-\pi/2, \pi/2)$$

be the spherical polar coordinates defining P_D. Typically one can choose the J2000 coordinate systems so that α is the right ascension and δ is the declination.

Definition 1 *An optical attributable vector is a vector*

$$A = (\alpha, \delta, \dot{\alpha}, \dot{\delta}) \in [-\pi, \pi) \times (-\pi/2, \pi/2) \times \mathbb{R}^2$$

observed at time t.

The optical attributable vector is precisely the set of coordinates that can be measured, from the observer's frame *on the Earth's surface*, at time t. Note that unless the debris particle is seen directly overhead, what we call a zenith measurement, this will translate into uncertainty in the polar angles of the geocentric frame. Since the coordinate transformation to the inertial, geocentric frame, depends on the position of the Earth, additional information will be stored along with the attributable vector. The full set of data that should be tabulated with each observation is:

$$x = (A, t, L) \in \mathbb{R}^5 \times \mathbb{N}$$

where $A = (\alpha, \delta, \dot{\alpha}, \dot{\delta})$ is the attributable vector, t is the time of observation, and L is observatory which made the observation (each observatory can be given integer-valued names). A function can then be defined as follows:

$$\psi : (t, L) \to (h, \Theta, \Phi)$$

where h is the altitude of the observatory (which we ignore in the current discussion), and (Θ, Φ) is the inertial angular location of observatory L at time t. The observation data x and inertial orientation function of the observatory ψ can then be unraveled to form the actual useable information for the coordinate transformations:

$$\mathfrak{X} = (A, t, h, \Theta, \Phi) \in \mathbb{R}^8$$

2.2 Measuring Attributable Vectors

One of the primary technical difficulties in Space Situational Awareness (SSA) is the inability to accurately estimate the full dynamical state of an object based on a single track of data. For example, optical search and survey telescopes will only observe objects for very short durations (minutes at most) [24]. This track of data contains information on the angular location of the satellite, but in general does not have sufficient information to allow for an accurate orbit determination of the object. For meaningful orbit characterization, the object must be observed again during a later pass. The problem, of course, is to discern which uncorrelated tracks are the same object.

Our approach to this problem is two-fold. First, as described in this section, is to extract the maximum amount of usable information from a single track of a space object and to also bound the possible domain of the unmeasured state components. Second, described in the next section, is to use this information to correlate one observation track with another from a previous observation in order to detect whether the two objects are the same. In the following we will focus specifically on optical observations of space debris, although the theory and analysis will also apply to radar observations of space debris. This focus is done solely for simplicity of presentation.

The challenge is to extract the maximum amount of usable information from a single track and also derive meaningful constraints on the remaining uncertainty aspects of the state. Instead of determining an overall covariance matrix for the object's state, based on a single track, that contains all 6 dimensions, our approach is to use the track observations to isolate those components of the object's state that can be constrained. For an optical track consisting of several angular observations over a time span of minutes these are the angular location and angular rate of the object at a specific epoch, generally chosen to lie within the track. The idea is to use the multiple angular measurements to develop an improved estimate of the angular location of the object and the angular rate of the object, and then use these measurements to constrain the unmeasured states of the object. This approach was recently proposed in [25] by Tommei et. al and is further extended in our research. While Tommei et al. discuss that a single track of optical data can determine the angle and angle rates of the object at a specific epoch, they did not outline how this determination could be made.

If, during an observation period, a space object passes through the field of view of an optical telescope, the optical telescope can take several measurements of that object, equivalent to a series of angles at specific times, the total time span being a number of minutes. We assume that these angles can be identified with each other to produce a single track of observable data for the space object. There is obviously more information in this pass of data than just a single fix of the angular location of the space object relative to the observer, however there is not enough information to provide an accurate orbit. To capture this additional information, we can estimate the space object's angular location, angular rate and angular acceleration at a fixed epoch, chosen within the tracking pass. The additional information content goes into reducing the uncertainty of the angle, angle-rate and angle-acceleration measurement at epoch. This approach recognizes that there is little information in one track related to the object range and range-rate, and concentrates on fixing the angles, angle-rates, and angle-accelerations to a higher level of precision.

In the following we provide an example of this approach for estimating a single angle and its associated rates. This can easily be expanded to a full estimate of both angles. At the heart of the approach is to estimate the kinematics of the angular motion of the object, in the Earth fixed frame, during the tracking pass. For simplicity in this example we assume the angular motion can be modeled kinematically as:

$$\alpha(t) \quad = \quad \alpha_o + \dot{\alpha}_o(t - t_o) + \frac{1}{2}\ddot{\alpha}_o(t - t_o)^2 \tag{1}$$

For a general application of this approach, higher order derivatives can be added and estimated and biases in the angular motion can also be added. The biases can only be estimated if tracks are compared between different objects. The problem then reduces to estimating the angular position, angular rate and angular acceleration of the object at time t_o. For simplicity in this example we assume 1-dimensional angular motion and a sequence of N equally spaced, uncorrelated observations centered on the epoch t_o and covering a time span T. This defines an estimation problem for the angle at epoch, α_o, the angular rate at epoch, $\dot{\alpha}_o$, and the angular acceleration at epoch, $\ddot{\alpha}_o$. There is sufficient information to estimate these provided there are at least 3 angle measurements in the track.

For simplicity we assume that the individual angle measurements are uncorrelated with each other. Then the least-squares estimation problem is to minimize the cost function

$$J = \frac{1}{2\sigma_\alpha^2}\sum_{i=1}^{N}\left(\alpha(t_i)-\alpha_i\right)^2 \tag{2}$$

where σ_α is the measurement uncertainty, α_i are the actual measurements and the $\alpha(t_i)$ are the predicted measurements. The quantities to estimate are $\alpha_o, \dot{\alpha}_o, \ddot{\alpha}_o$. Forming the necessary equations, and using the fact that $\alpha(t)$ is linear in the quantities to estimate, we form the normal equations:

$$\Lambda\begin{bmatrix}\alpha_o\\ \dot{\alpha}_o\\ \ddot{\alpha}_o\end{bmatrix} = d \tag{3}$$

$$\Lambda = \sum_{i=1}^{N}\frac{1}{\sigma_\alpha^2}\begin{bmatrix}1 & t_i-t_o & \frac{1}{2}(t_i-t_o)^2\\ t_i-t_o & (t_i-t_o)^2 & \frac{1}{2}(t_i-t_o)^3\\ \frac{1}{2}(t_i-t_o)^2 & \frac{1}{2}(t_i-t_o)^3 & \frac{1}{4}(t_i-t_o)^4\end{bmatrix} \tag{4}$$

$$d = \sum_{i=1}^{N}\frac{\alpha_i}{\sigma_\alpha^2}\begin{bmatrix}1\\ t_i-t_o\\ \frac{1}{2}(t_i-t_o)^2\end{bmatrix} \tag{5}$$

To characterize the information content in a single pass of data, we can explicitly compute the Information Matrix Λ. To do this we assume the measurements are taken at equal times $t_i = t_o + \frac{T}{2n}i$ where $i = -n, -(n-1), \ldots, -1, 0, 1, \ldots, n$, forming a total of $2n+1$ measurements over the time-span T. Due to this assumption, the odd terms will all sum to zero:

$$\Lambda = (2n+1)\begin{bmatrix}1 & 0 & \frac{n(n+1)}{6}\left(\frac{T}{2n}\right)^2\\ 0 & \frac{n(n+1)}{3}\left(\frac{T}{2n}\right)^2 & 0\\ \frac{n(n+1)}{6}\left(\frac{T}{2n}\right)^2 & 0 & \frac{n(n+1)(3n^2+3n-1)}{60}\left(\frac{T}{2n}\right)^4\end{bmatrix} \tag{6}$$

The inverse of this is the covariance matrix, $P = \Lambda^{-1}$, and has information on the accuracy to which the angle quantities are measured. To simplify the computation, assume that $n \gg 1$ (often not a valid assumption) and invert the matrix to find:

$$P = \frac{\sigma_\alpha^2}{(2n+1)}\begin{bmatrix}\frac{9}{4} & 0 & -\frac{15}{2}\left(\frac{2}{T}\right)^2\\ 0 & 3\left(\frac{2}{T}\right)^2 & 0\\ -\frac{15}{2}\left(\frac{2}{T}\right)^2 & 0 & 45\left(\frac{2}{T}\right)^4\end{bmatrix} \tag{7}$$

With the approximate determinations of:

$$\sigma_{\alpha_o} \sim \frac{3\sigma_\alpha}{2\sqrt{N}} \tag{8}$$

$$\sigma_{\dot{\alpha}_o} \sim \frac{2\sqrt{3}\sigma_\alpha}{T\sqrt{N}} \tag{9}$$

$$\sigma_{\ddot{\alpha}_o} \sim \frac{12\sqrt{5}\sigma_\alpha}{T^2\sqrt{N}} \tag{10}$$

and a correlation between the angle and angular acceleration uncertainties. Now consider some published tracking data characteristics for the MODEST space surveillance telescope which tracks GEO objects [24]. A usual pass lasts for 5 minutes during which they take $N = 8$ observations. Several published reports indicate optical sensors have 1 arcsecond or 2.8×10^{-4} deg observation uncertainties, which we use for σ_α. Putting these numbers together, this implies that such a track of observations contains information on the angular location and angular rate of the object at epoch t_o with errors on the order of $\sigma_{\alpha_o} \sim 1.5 \times 10^{-4\circ}$, $\sigma_{\dot{\alpha}_o} \sim 1 \times 10^{-6\circ}/\mathrm{s}$ and $\sigma_{\ddot{\alpha}_o} \sim 3 \times 10^{-8\circ}/\mathrm{s}^2$.

This approach combines the information from a track of observations spread out in time and transforms it into a precise estimate of the partial state of the object at a specific epoch. This is a more convenient form in which to transform the information from the track and makes it easier to discuss constraints on the unmeasured components of the space object's state. For an optical observation these unmeasured components are the object's range and range-rate at the epoch t_o and define the attributable vector A.

2.3 The Admissible Region

The specific geocentric energy of the particle is

$$E = \frac{1}{2}||\dot{P}||^2 - \frac{\mu}{||P||}$$

where $\mu = GM_\oplus$ is the gravitational parameter of the Earth, and we take $G = 19.91\ \mathrm{R}_\oplus^3 \mathrm{M}_\oplus^{-1} \mathrm{hr}^{-1}$.

Given an optical attributable vector A, its corresponding *admissible region* is the set of points on the $(\rho, \dot{\rho})$ plane that have not been ruled out by physical considerations. We impose the following physical constraints on the possible positions of the particle in the topocentric range/range-rate $(\rho, \dot{\rho})$ plane:

- $\mathcal{C}_1 = \{(\rho, \dot{\rho}) : E < 0\}$
- $\mathcal{C}_2 = \{(\rho, \dot{\rho}) : 2 < \rho < 20\}$
- $\mathcal{C}_3 = \{(\rho, \dot{\rho}) : 1.03 < r_p\}$
- $\mathcal{C}_4 = \{(\rho, \dot{\rho}) : r_a < 25\}$

where r_p and r_a are the periapsis and apoapsis (geocentric) radii of the orbit, respectively; and where distance is measured in units of Earth-radii. $\mathcal{C}_1$ and $\mathcal{C}_2$ are the constraints as presented in Tommei et al. [25], and $\mathcal{C}_3$ and $\mathcal{C}_4$ are two additional physical constraints we now place on the admissible region by constraining the periapsis and apoapsis (geocentric) radii of the orbit to always lie within some range. These latter constraints place a restriction on the possible eccentricities of the orbit, which rules out impact orbits and orbits with an extremely high apoapsis. A periapsis of

1.03 corresponds to a periapsis radius at about 200 km above the surface of the Earth. The admissible region is then defined as a subset of the topocentric range/range-rate plane by the condition:

$$\mathcal{C} = \bigcap_{i=1}^{4} \mathcal{C}_i \tag{11}$$

In order to compute the periapsis and apoapsis radii of the orbit, one must transfer to geocentric coordinates. In coordinates, we have:

$$\hat{R} = \langle \cos\alpha\cos\delta, \sin\alpha\cos\delta, \sin\delta \rangle, \qquad \hat{R}_\alpha := \frac{\partial \hat{R}}{\partial \alpha}, \qquad \hat{R}_\delta := \frac{\partial \hat{R}}{\partial \delta}$$

Then:

$$\begin{aligned} P &= P_O + \rho\hat{R} & (12) \\ \dot{P} &= \dot{P}_O + \dot{\rho}\hat{R} + \rho\dot{\alpha}\hat{R}_\alpha + \rho\dot{\delta}\hat{R}_\delta & (13) \end{aligned}$$

does the trick.

To illustrate the improvement the additional constraint $\mathcal{C}_3 \cap \mathcal{C}_4$ makes, we consider the following example attributable vector. Suppose the optical observer's position in standard coordinates is polar angle $\Theta = \pi/3$ (measured as the polar angle from the north pole) and azimuthal angle $\Phi = 0$ (measured from inertial x-axis), and the observer makes the following zenith observation $A = (0, \pi/6, 0.1, 0.03)$. Fig. 1 shows the resulting admissible region. The outlined region is the admissible region presented in Tommei et al. [25], i.e. $\mathcal{C}_{\text{tom}} = \mathcal{C}_1 \cap \mathcal{C}_2$. The inside dotted region is the (discretized) admissible region as presented here, i.e. $\mathcal{C} = \mathcal{C}_1 \cap \mathcal{C}_2 \cap \mathcal{C}_3 \cap \mathcal{C}_4$. As one can see, these additional constraints significantly reduces the area of the admissible region that one must consider in making the orbit determination.

3 Delaunay Variables

In this section, we will define the set of canonical Delaunay variables that we will use and then indicate how one would compute the corresponding State Transition Matrix (STM).

3.1 Transformation to Delaunay Variables

One can transfer the uncertainty surface (admissible region) into geocentric cartesian coordinates and then let each point of this surface evolve as a Kepler orbit. If one does so, one sees that the surface spreads out fairly quickly. As an alternative, we will transfer the surface into Delaunay variables. This is done in several steps. We first transfer the topocentric spherical observation coordinates into geocentric cartesian coordinates using (12)-(13):

$$T_1 : \langle \rho, \dot{\rho}, \mathfrak{X} \rangle \to \langle x, y, z, \dot{x}, \dot{y}, \dot{z} \rangle$$

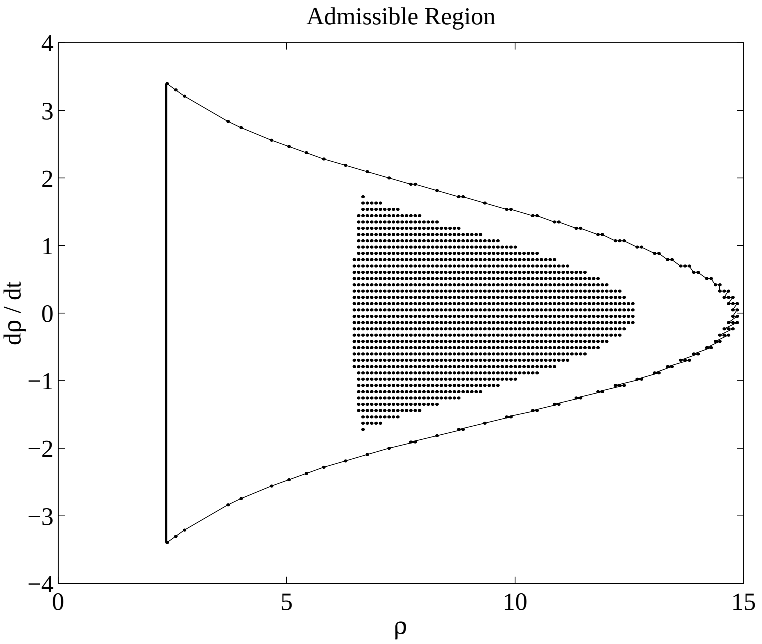

Figure 1: Admissible Region for attributable vector $A = (0, \pi/6, 0.1, 0.03)$, zenith measurement

This transformation depends on the full set of recorded data $\mathfrak{X} = (A, t, h, \Theta, \Phi)$, as it depends on the location of the observer at that time. As usual, $A = \langle \alpha, \delta, \dot{\alpha}, \dot{\delta} \rangle$ is the admissible vector associated with a given track of data. Next, we transfer the cartesian coordinates into a set of orbital elements, using standard relations (see Danby [7], Roy [22], Crassidis & Junkins [6], Montenbruck & Gill [19], etc.).

$$T_2 : \langle x, y, z, \dot{x}, \dot{y}, \dot{z} \rangle \rightarrow \langle a, e, i, \omega, \Omega, M \rangle$$

where a is the semi-major axis, e is the eccentricity, i is the inclination, ω is the argument of periapsis, Ω is the longitude of the ascending node, and M is the mean anomaly. Lastly we transfer the orbital elements into Delaunay variables.

$$T_3 : \langle a, e, i, \omega, \Omega, M \rangle \rightarrow \langle L, l, G, g, H, h \rangle$$

where the Delaunay variables are defined as in Ferraz-Mello [10]:

$$\begin{aligned} l &= M, & L &= \sqrt{\mu a}, \\ g &= \omega, & G &= L\sqrt{1 - e^2}, \\ h &= \Omega, & H &= G \cos i, \end{aligned} \tag{14}$$

so that the total transformation from the observation space to Delaunay space at the initial time t_0 is given by the composition:

$$T(t_0; t_0) = T_3 \circ T_2 \circ T_1 \tag{15}$$

The reason for this seemingly superfluous notation, i.e. $T(t_0; t_0)$, will be made clear by the end of the section. For the case of zero-eccentricity or zero-inclination orbits, the Delaunay variables become singular, and one could instead choose Poincaré nonsingular canonical variables:

$$T_3' : \langle a, e, i, \omega, \Omega, M \rangle \rightarrow \langle \mathfrak{l}, \mathfrak{L}, \mathfrak{g}, \mathfrak{G}, \mathfrak{h}, \mathfrak{H} \rangle$$

$$\begin{aligned} \mathfrak{l} &= M + \omega + \Omega, & \mathfrak{L} &= L = \sqrt{\mu a} \\ \mathfrak{g} &= \omega + \Omega & \mathfrak{G} &= G - L = L(\sqrt{1-e^2} - 1) \\ \mathfrak{h} &= \Omega & \mathfrak{H} &= H - G = G(\cos i - 1) \end{aligned}$$

For simplicity, we will restrict our attention to cases where singularities are not present and one can use Delaunay variables.

We choose Delaunay variables because, like the orbital elements, five of them are constants of motion for the unperturbed Kepler problem. Additionally, unlike the orbital elements, there is a natural pairing of the Delaunay variables because they occur in coordinate-momenta symplectic pairs, i.e. the Delaunay variables l, g, and h are angle variables, to be modded by 2π, and L, G, and H are action variables, or the conjugate momenta. In terms of the Delaunay variables, the equations of motion of the system reduce to Hamilton's equations:

$$\begin{aligned} \frac{dl}{dt} &= \frac{\partial \mathcal{F}}{\partial L} & \frac{dL}{dt} &= -\frac{\partial \mathcal{F}}{\partial l} \\ \frac{dg}{dt} &= \frac{\partial \mathcal{F}}{\partial G} & \frac{dG}{dt} &= -\frac{\partial \mathcal{F}}{\partial g} \\ \frac{dh}{dt} &= \frac{\partial \mathcal{F}}{\partial H} & \frac{dH}{dt} &= -\frac{\partial \mathcal{F}}{\partial h} \end{aligned} \tag{16}$$

where

$$\mathcal{F} = -\frac{\mu^2}{2L^2} + \mathcal{R}(L, l, G, g, H, h)$$

and where $\mathcal{R}(L, l, G, g, H, h)$ is the disturbing force expressed in terms of Delaunay variables. For the unperturbed Kepler problem, the equations of motion work out as:

$$\frac{dl}{dt} = \frac{\mu^2}{L^3}, \qquad \frac{dL}{dt} = \frac{dH}{dt} = \frac{dG}{dt} = \frac{dh}{dt} = \frac{dg}{dt} = 0 \tag{17}$$

For the general case, we can denote the Hamiltonian flow of (16) as:

$$T_4(t; t_0) : \langle L(t_0), l(t_0), G(t_0), g(t_0), H(t_0), h(t_0) \rangle \rightarrow \langle L(t), l(t), G(t), g(t), H(t), h(t) \rangle$$

For the Kepler problem, this simplifes to the form:

$$T_4^{\text{kepler}}(t; t_0)(L_0, l_0, G_0, g_0, H_0, h_0) = \left\langle L_0, \left(l_0 + \frac{\mu^2}{L_0^3}(t - t_0) \right), G_0, g_0, H_0, h_0 \right\rangle$$

The transformation from the observation space to the time-evolved Delaunay space is then given by:

$$T(t;t_0) = T_4(t;t_0) \circ T(t_0;t_0) \tag{18}$$

where $T(t_0;t_0)$ is defined in (15). This is well-defined because $T_4(t_0;t_0)$ is the identity transformation.

3.2 The Jacobian Matrix

As we shall see, the Jacobian Matrix of the transformation T will be used to compute variations in the Delaunay variables with respect to variations in the $(\rho, \dot{\rho})$ plane. Since the variables $(\alpha, \dot{\alpha}, \delta, \dot{\delta})$ are taken to be known, we only need consider the first two columns of the Jacobian of T. We will denote this 6×2 matrix as Φ. We construct Φ by composition. First we define:

$$\Phi_1 = \frac{\partial(x,y,z,\dot{x},\dot{y},\dot{z})}{\partial(\rho,\dot{\rho})} = \begin{bmatrix} \cos\alpha\cos\delta & 0 \\ \sin\alpha\cos\delta & 0 \\ \sin\delta & 0 \\ -\dot{\alpha}\sin\alpha\cos\delta - \dot{\delta}\cos\alpha\sin\delta & \cos\alpha\cos\delta \\ \dot{\alpha}\cos\alpha\cos\delta - \dot{\delta}\sin\alpha\sin\delta & \sin\alpha\cos\delta \\ \dot{\delta}\cos\delta & \sin\delta \end{bmatrix}$$

where the partial derivatives have been computed using the transformation relations (12)-(13).

Next, the Jacobian of the transformation T_2 is computed:

$$\Phi_2 = \frac{\partial(a,e,i,\omega,\Omega,M)}{\partial(x,y,z,\dot{x},\dot{y},\dot{z})}$$

A very efficient and elegant algorithm to compute this matrix is given in Montenbruck & Gill [19], §7.1.2 - §7.1.3. Since this computation is well known, we will not go through the details of it here.

The Jacobian of the transformation matrix T_3 is then computed:

$$\Phi_3 = \frac{\partial(L,l,G,g,H,h)}{\partial(a,e,i,\omega,\Omega,M)} = \begin{bmatrix} L_a & 0 & 0 & 0 & 0 & 0 \\ 0 & 0 & 0 & 0 & 0 & 1 \\ L_a\sqrt{1-e^2} & G_e & 0 & 0 & 0 & 0 \\ 0 & 0 & 0 & 1 & 0 & 0 \\ L_a\sqrt{1-e^2}\cos i & G_e\cos i & -G\sin i & 0 & 0 & 0 \\ 0 & 0 & 0 & 0 & 1 & 0 \end{bmatrix}$$

where

$$L_a = \frac{1}{2}\sqrt{\frac{\mu}{a}} \qquad \text{and} \qquad G_e = \frac{-Le}{\sqrt{1-e^2}}$$

Finally, the Jacobian corresponding to the time evolution of the system (16) can be found using standard techniques (see Maruskin et al. [15] for the procedure):

$$\Phi_4(t;t_0) = \frac{\partial(L(t), l(t), G(t), g(t), H(t), h(t))}{\partial(L(t_0), l(t_0), G(t_0), g(t_0), H(t_0), h(t_0))}$$

This Jacobian Matrix, since it corresponds to a time evolution transformation, is also known as the State Transition Matrix (STM) of the evolution map. For the Kepler case, this STM takes the simple analytic form:

$$\Phi_4^{\mathrm{kepler}}(t;t_0) = \begin{bmatrix} 1 & 0 & 0 & 0 & 0 & 0 \\ -3\mu^2(t-t_0)/L_0^4 & 1 & 0 & 0 & 0 & 0 \\ 0 & 0 & 1 & 0 & 0 & 0 \\ 0 & 0 & 0 & 1 & 0 & 0 \\ 0 & 0 & 0 & 0 & 1 & 0 \\ 0 & 0 & 0 & 0 & 0 & 1 \end{bmatrix} \tag{19}$$

The 6×2 matrix Φ, which is the first 2 columns of the Jacobian of T, is then given by:

$$\Phi(t;t_0) = \Phi_4(t;t_0) \cdot \Phi_3 \cdot \Phi_2 \cdot \Phi_1$$

and it maps a variation in the admissible region to a variation in the Delaunay variables, i.e.

$$\begin{bmatrix} \delta L \\ \delta l \\ \delta G \\ \delta g \\ \delta H \\ \delta h \end{bmatrix} = \Phi_{6\times 2} \cdot \begin{bmatrix} \delta\rho \\ \delta\dot{\rho} \end{bmatrix}$$

Additionally, the following three 2×2 symplectic submatrices of $\Phi(t;t_0)$ will be considered:

$$\begin{aligned} \mathbb{L}(t;t_0) &= \begin{bmatrix} I_2 & 0_2 & 0_2 \end{bmatrix} \cdot \Phi(t;t_0) \\ \mathbb{G}(t;t_o) &= \begin{bmatrix} 0_2 & I_2 & 0_2 \end{bmatrix} \cdot \Phi(t;t_0) \\ \mathbb{H}(t;t_0) &= \begin{bmatrix} 0_2 & 0_2 & I_2 \end{bmatrix} \cdot \Phi(t;t_0) \end{aligned}$$

where 0_2 and I_2 are the 2×2 matrix of zeros and identity matrix, respectively. These are defined so that:

$$\begin{bmatrix} \delta L \\ \delta l \end{bmatrix} = \mathbb{L} \cdot \begin{bmatrix} \delta\rho \\ \delta\dot{\rho} \end{bmatrix}, \qquad \begin{bmatrix} \delta G \\ \delta g \end{bmatrix} = \mathbb{G} \cdot \begin{bmatrix} \delta\rho \\ \delta\dot{\rho} \end{bmatrix}, \qquad \text{and} \qquad \begin{bmatrix} \delta H \\ \delta h \end{bmatrix} = \mathbb{H} \cdot \begin{bmatrix} \delta\rho \\ \delta\dot{\rho} \end{bmatrix}$$

Notice that, because of the especially simple form $\Phi_4(t;t_0)$ takes in the Kepler case (19), the dynamic time evolution of the system *only affects the submatrix* $\mathbb{L}$ of the full STM $\Phi(t;t_0)$. Thus, once the matrices $\mathbb{G}$ and $\mathbb{H}$ are computed for a VD particle, they are constant in time. Note that they still depend on the VD particle, as they depend on $\alpha, \dot{\alpha}, \delta, \dot{\delta}, \rho, \dot{\rho}$, the location of the optical observer on Earth, and the time of the measurement (which gives the observer's position in *inertial* space).

4 Intersection Theory Analysis (ITA)

In this section we describe how the Delaunay space can be used in fitting an orbit determination between two previously uncorrelated tracks (UCT's). In subsequent sections we will illustrate this technique for a sample set of observations, considering separately zenith and non-zenith observations, and additionally the effect of the J_2 term in Earth's potential on the proposed orbit determination process.

4.1 Mapping the Admissible Region to Delaunay Space

Let $\mathcal{D} \cong \mathbb{R}^6$ be six-dimensional Delaunay space and $\mathcal{C}(\mathfrak{X})$ the admissible region for a fixed attributable vector and spatiotemporal observation location, as defined in (11). For a fixed epoch time τ, we define the map $F^\tau_{\mathfrak{X}} : \mathcal{C} \to \mathcal{D}$ as the restriction of the map $T(\tau; t)$ defined in (18) for a fixed $\mathfrak{X}$, where t is the time of the observation (one of the components of $\mathfrak{X}$), so that:

$$F^\tau_{\mathfrak{X}} : \langle \rho, \dot{\rho} \rangle \to \langle L, l, G, g, H, h \rangle$$

Thus $F^\tau_{\mathfrak{X}}(\mathcal{C}) \subset \mathcal{D}$ is a two-dimensional submanifold of Delaunay space $\mathcal{D} \cong \mathbb{R}^6$. We further define the three *Delaunay projective spaces* $\mathcal{D}_L \cong \mathcal{D}_G \cong \mathcal{D}_H \cong \mathbb{R}^2$, so that the Delaunay space $\mathcal{D}$ has the direct sum decomposition $\mathcal{D} = \mathcal{D}_L \oplus \mathcal{D}_G \oplus \mathcal{D}_H$. These three projective spaces are the projections of Delaunay space onto the three symplectic Delaunay planes. If Π_L, Π_G, and Π_H are the projection operators from the full six-dimensional Delaunay space onto the symplectic Delaunay planes, so that $\Pi_L(L, l, G, g, H, h) = \langle L, l \rangle$, etc., then $\mathcal{D}_L = \Pi_L(\mathcal{D})$, $\mathcal{D}_G = \Pi_G(\mathcal{D})$, and $\mathcal{D}_H = \Pi_H(\mathcal{D})$. The map $F^\tau_{\mathfrak{X}}$ can thus be thought of in either of two ways, as a one-to-one mapping from the two-dimensional admissible region $\mathcal{C}$ to the six-dimensional Delaunay space $\mathcal{D}$ or as a one-to-three mapping from the two-dimensional admissible region $\mathcal{C}$ to the three two-dimensional Delaunay projective spaces $\mathcal{D}_L$, $\mathcal{D}_G$, and $\mathcal{D}_H$. While at first glance, such a distinction seems pedantic, it is actually an important one, as intersections are inherently easier to both visualize and carry out in two-dimensional spaces then they are in six-dimensional spaces.

4.2 Necessary Conditions for Correlation between 2 UCT's

As discussed previously, each uncorrelated track (UCT) provides a set of data $\mathfrak{X}$ that contains the attributable vector and information on when and where the observatory was at the time of the measurements of the track. The Space Situational Awareness (SSA) problem is to determine which UCT's belong to the same physical object, carry out an orbit determination for each orbit, and then to add known orbits to the space debris catalog. In this section we discuss how to compare pairwise UCT's to determine whether they correlate to the same object.

Given two extended attributable vectors $\mathfrak{X}_1$ and $\mathfrak{X}_2$, one determines the corresponding admissible regions $\mathcal{C}_1$ and $\mathcal{C}_2$, respectively. These admissible regions cannot be compared directly, as they are subsets of two different sets of topocentric spherical coordinates, affixed to the Earth at different locations and different times. Even if both attributable vectors were recorded by the same observatory, if the time between the two tracks, modulo 24 hours, is not zero, that single observatory would have been at two different positions in inertial space when it measured the two different tracks. We now push the admissible regions forward into Delaunay space, and dynamically evolve or regress both uncertainty distributions in time to a common epoch τ, so that $F^{\tau}_{\mathfrak{X}_1}(\mathcal{C}_1)$ and $F^{\tau}_{\mathfrak{X}_2}(\mathcal{C}_2)$ are both two-dimensional submanifolds of six-dimensional Delaunay space $\mathcal{D}$, dynamically mapped to a common epoch time.

If $\mathfrak{X}_1$ and $\mathfrak{X}_2$ correspond to the same object, then $F^{\tau}_{\mathfrak{X}_1}(\mathcal{C}_1) \bigcap F^{\tau}_{\mathfrak{X}_2}(\mathcal{C}_2) \neq \emptyset$.

Since $\mathfrak{X}_1$ and $\mathfrak{X}_2$ each contain four pieces of information (two angles and two angle rates), the system is overdetermined. Unless there is some redundancy in the information, if both tracks correspond to the same physical object, it is likely that the uncertainty manifolds $F^{\tau}_{\mathfrak{X}_1}(\mathcal{C}_1)$ and $F^{\tau}_{\mathfrak{X}_2}(\mathcal{C}_2)$ will intersect at a single point.

Suppose now that this is the case, i.e. the intersection $F^{\tau}_{\mathfrak{X}_1}(\mathcal{C}_1) \bigcap F^{\tau}_{\mathfrak{X}_2}(\mathcal{C}_2) = \{\mathbf{\Delta}^*\}$ is at the single point $\mathbf{\Delta}^* \in \mathcal{D}$. Then the two extended attributable vectors $\mathfrak{X}_1$ and $\mathfrak{X}_2$ corresponding to the two separate UCT's do *not necessarily belong* to the same object. Rather one can say two things. If they belong to the same object, that object's orbit is given by $\mathbf{\Delta}^*$. Secondly, they almost certainly do belong to the same object. This is more deeply expounded over the next several paragraphs.

They do not necessarily correlate to the same object for the following reason. The orbit corresponding to the first UCT can still lie anywhere on $F^{\tau}_{\mathfrak{X}_1}(\mathcal{C}_1)$ and the orbit corresponding to the second UCT can still lie anywhere on $F^{\tau}_{\mathfrak{X}_1}(\mathcal{C}_1)$. We do not yet know the two UCT's correlate to the same object, so even though both uncertainty manifolds intersect at a single point, this may not be the correct orbit for either object.

They almost certainly do belong to the same object for the following reason. $F^{\tau}_{\mathfrak{X}_1}(\mathcal{C}_1)$ and $F^{\tau}_{\mathfrak{X}_1}(\mathcal{C}_1)$ are two separate two-dimensional manifolds embedded into the same six-dimensional Delaunay space $\mathcal{D}$. The probability that they, *by accident*, happen to touch tangentially at a single intersection point $\mathbf{\Delta}^*$ is extremely low, unless they are correlated and the orbit for both objects is given by that common intersection point $\mathbf{\Delta}^*$. One can therefore, with great confidence, make a preliminary orbit determination from $\mathbf{\Delta}^*$ and consider the two tracks as correlated. One then places this preliminary orbit determination into a separate holding catalog and awaits confirmation by a third consistent track of data, at which time the orbit is added to the standard catalog.

The topic of determining this intersection point is taken up in the following subsection.

4.3 Intersection Theory Analysis

Supposing two extended attributable vectors $\mathfrak{X}_1$ and $\mathfrak{X}_2$ correspond to the same physical object, a unique intersection point $\mathbf{\Delta}^*$ of the two submanifolds $F^{\tau}_{\mathfrak{X}_1}(\mathcal{C}_1)$ and $F^{\tau}_{\mathfrak{X}_1}(\mathcal{C}_1)$

can be found. To do this, we will consider the three-fold projection of these surfaces onto the Delaunay planes. To reduce complexity of notation let us define

$$\begin{aligned} S^i_L &= \Pi_L(F^{\tau}_{\mathfrak{X}_i}(\mathcal{C}_i)) \subset \mathcal{D}_L \\ S^i_G &= \Pi_G(F^{\tau}_{\mathfrak{X}_i}(\mathcal{C}_i)) \subset \mathcal{D}_G \\ S^i_H &= \Pi_H(F^{\tau}_{\mathfrak{X}_i}(\mathcal{C}_i)) \subset \mathcal{D}_H \end{aligned}$$

For each of the symplectic Delaunay surface projections, there is an overlap region

$$S^1_L \cap S^2_L \qquad\qquad S^1_G \cap S^2_G \qquad\qquad S^1_H \cap S^2_H$$

See, for example, Fig. 8 (the overlap regions are not highlighted). We know that if the two tracks were of the same object, the true orbit must be in each of these intersected regions, i.e. $\Pi_L(\mathbf{\Delta}^*) \in S^1_L \cap S^2_L$ and similarly for the G and H projections. However, since each projection is a unique view of the same two two-dimensional surfaces, more information can be extracted. To obtain the unique intersection point, one carries out the following algorithm, which we have named Intersection Theory Analysis (ITA):

1. Select a Delaunay plane P, where $P \in \{\text{“}L\text{”}, \text{“}G\text{”}, \text{“}H\text{”}\} \subset$ the alphabet.

2. The projection of $\mathbf{\Delta}^*$ must lie in the intersection of the two projected uncertainty surfaces, i.e. $\mathbf{\Delta}^* \in S^1_P \cap S^2_P$. Both projections S^1_P and S^2_P are discretized by a population of virtual debris (VD) particles that have been mapped into the Delaunay space. Omit all VD particles that do not lie in the overlap region. Now define
$$\diamond F^{\tau}_{\mathfrak{X}_i}(\mathcal{C}_i) \subset F^{\tau}_{\mathfrak{X}_i}(\mathcal{C}_i) \subset \mathcal{D}$$
by the relation
$$\Pi_P(\diamond F^{\tau}_{\mathfrak{X}_i}(\mathcal{C}_i)) = S^1_P \cap S^2_P$$

3. Now reproject both surfaces $\diamond F^{\tau}_{\mathfrak{X}_1}(\mathcal{C}_1)$ and $\diamond F^{\tau}_{\mathfrak{X}_2}(\mathcal{C}_2)$ onto the Delaunay planes. Define their projections as:
$$\begin{aligned} \diamond S^i_L &= \Pi_L(\diamond F^{\tau}_{\mathfrak{X}_i}(\mathcal{C}_i)) \subset \mathcal{D}_L \\ \diamond S^i_G &= \Pi_G(\diamond F^{\tau}_{\mathfrak{X}_i}(\mathcal{C}_i)) \subset \mathcal{D}_G \\ \diamond S^i_H &= \Pi_H(\diamond F^{\tau}_{\mathfrak{X}_i}(\mathcal{C}_i)) \subset \mathcal{D}_H \end{aligned}$$
See Fig. 9 for an example of this. Notice that, in this figure, all nonoverlap points on the Delaunay plane $\mathcal{D}_H$ have been omitted.

4. Repeat Steps 1-3. For step 1 choose a different P. It is all right if you've used that P before, as long as you do not use the same P twice. For steps 2-3, add an extra diamond to each strand of diamonds to indicate that an additional reduction has taken place. Continue until you are left with a single (approximate) intersection point.

The diamond operator is identified with omitting all nonoverlap regions in a particular Delaunay plane. The process of orbit determination is therefore reduced to the development of an efficient computer algorithm that will determine this overlap region for two overlapping discretized laminas on $\mathbb{R}^2$. This procedure is illustrated over the next several sections of the paper, as an initial feasibility study of the ITA algorithm. For the current work, the overlap regions were computed by manual computation and by trial and error. Creating a computer algorithm that determines these overlap regions automatically will be a focus of future research.

5 Orbit Determination I: Kepler Orbit with 2 Zenith Observations

5.1 Concurrent Plot of 2 Zenith Observations on the Delaunay Planes

In this section we consider the admissible region corresponding to the zenith observation $A = (0, \pi/6, 0.1, 0.03)$, made at $t = 0$ from a point on the Earth's surface $\Theta = \pi/3$, $\Phi = 0$. The admissible region of the $(\rho, \dot{\rho})$ plane is the inner discretized region plotted in Fig. 1. Each district of the discretization is referred to as a VD particle. We will think of the uncertainty region as a two-dimensional surface in a six-dimensional space:

$$\mathcal{A} := \{\langle \rho, \dot{\rho}, \alpha, \delta, \dot{\alpha}, \dot{\delta}\rangle : (\alpha, \delta, \dot{\alpha}, \dot{\delta}) = A \text{ and } (\rho, \dot{\rho}) \in \mathcal{C}\}$$

where $\mathcal{C}$ is the admissible region defined in (11). We call $\mathcal{C}$ the admissible region of the $(\rho, \dot{\rho})$ plane and $\mathcal{A}$ the admissible region of the observation space. Define:

$$T_1\{\mathcal{A}\} := \{\langle r, \dot{r}\rangle \in \mathbb{R}^6 : T_1^{-1}(\langle r, \dot{r}\rangle) \in \mathcal{A}\},$$

i.e. $T_1\{\mathcal{A}\}$ is the image of $\mathcal{A}$ under the mapping T_1. Then $T_1\{\mathcal{A}\}$ is a two-dimensional surface in the geocentric cartesian phase space. Similarly, we define:

$$T(t; t_0)\{\mathcal{A}\} := \{x = \langle L, l, G, g, H, h\rangle \in \mathbb{R}^6 : T(t; t_0)^{-1} \cdot x \in \mathcal{A}\}$$

where $T(t; t_0)$ is defined by the relations in §3.1. $T(t; t_0)\{\mathcal{A}\}$ is a two-dimensional surface in Delaunay space. Since $T_1\{\mathcal{A}\}$ is allowed to move about relatively freely, fold, wrap around the planet, etc., we will choose to follow the dynamic evolution of the surface $T(t; t_0)\{\mathcal{A}\}$ instead, which has a much more restricted evolution.

The projections of $T(0; 0)\{\mathcal{A}\}$ onto the three symplectic Delaunay planes are shown in Fig. 2. Since the phase flow is Hamiltonian and the Delaunay variables are a set of coordinate-momentum symplectic pairs, the sum of the oriented area projections onto the Delaunay planes is conserved, Arnold [2], Marsden & Ratiu [13], Maruskin et al. [14, 15]. Since all of the Delaunay variables except for l are constants of motion for the Kepler problem, the total area projection on the $(L - l)$ Delaunay

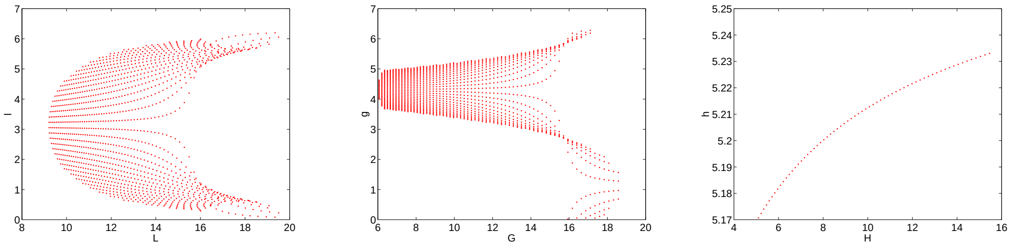

Figure 2: $T(0;0)\{\mathcal{A}\}$ projected onto the Delaunay planes

plane will be conserved, unless the surface "folds over," as was discussed in Scheeres et al. [23]. Because the observation was made directly overhead, a certain degeneracy exists that causes the projection of the uncertainty region on the (H, h) Delaunay plane to be a line, as in Fig. 2.

The dynamics for the Kepler problem, in terms of Delaunay variables, is governed by the equations of motion (17). In particular, $dl/dt \propto L^{-3}$. All of the dots in the (L, l) plane will march up the graph. Since the angle l is given modulo 2π, when a dot reaches $l = 2\pi$, it is reset to $l = 0$. The regions for smaller L will move at a greater constant rate than the regions for larger L. In this way a shearing effect takes place. The dynamics literally shreds the region into thin strips. The longer you wait, the more thin strips the uncertainty region will be cut up into. After 70 hrs, the surface $T(70;0)\{\mathcal{A}\}$ is projected onto the symplectic Delaunay planes, and is shown in Fig. 3. Notice the projections onto the (G, g) and (H, h) plane are unchanged.

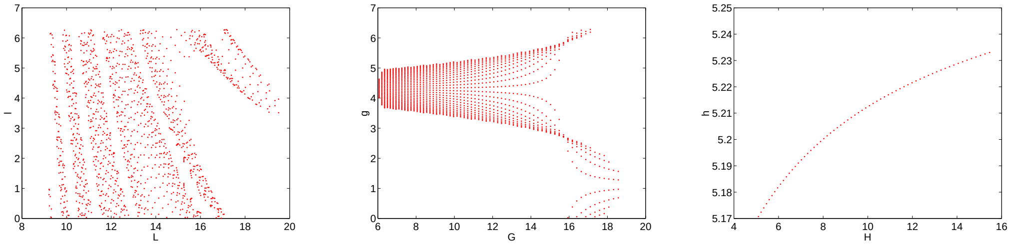

Figure 3: $T(70;0)\{\mathcal{A}\}$ projected onto the Delaunay planes

At time $t = 70$ hrs we will assume that we have another zenith observation of the same particle of space debris. MATLAB randomly selected VD field particle #893 to correspond to the actual physical piece of debris. If VD particle #893 were to be observed again at time $t = 70$ by an Earthbound optical observer with inertial polar angle $\Theta = 1.1650$ (measured from the north pole) and azimuthal angle $\Phi = 5.9214$ (measured from the inertial x-axis), its attributable vector would be $A_{70} = (\alpha, \delta, \dot{\alpha}, \dot{\delta}) = (-0.3618, 0.4058, 0.0315, 0.0209)$. Since $\alpha = \Phi - 2\pi$ and $\delta = \pi/2 - \Theta$, this is again a zenith observation. For this second observation, $t_0 = 70$, so the initial transformation of the admissible region of the observation space $\mathcal{A}_{70}$ to the Delaunay space would be $T(70;70)\{\mathcal{A}_{70}\}$. $\mathcal{A}_{70}$ is the *new* observation recorded at time $t = 70$. $T(70;0)\{\mathcal{A}\}$ and $T(70;70)\{\mathcal{A}_{70}\}$ are plotted concurrently on each of the Delaunay planes in Fig. 4.

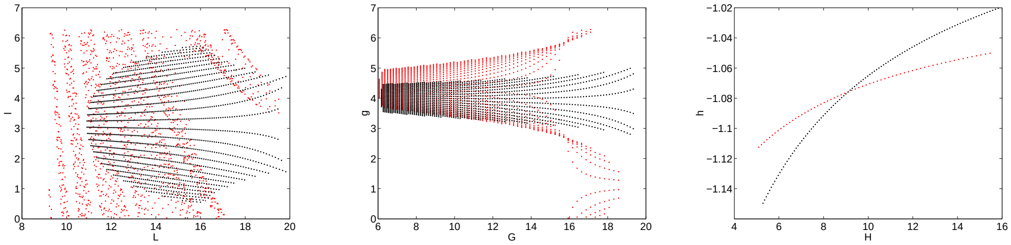

Figure 4: $T(70;0)\{\mathcal{A}\}$ (red) and $T(70;70)\{\mathcal{A}_{70}\}$ (black) projected onto the Delaunay planes.

The intersection of the two lines in the $(H - h)$ plane in Fig. 4 indicates that the Delaunay variables H and h can be determined exactly. This reduces the uncertainty region to a one-dimensional uncertainty curve, since each point on each line in the (H, h) plane is a curve in the original $(\rho, \dot{\rho})$ admissible region.

5.2 Determining the Intersection Point on the $(H - h)$ Plane

As earlier noted, if both observations are zenith observations, the uncertainty region projected onto the $(H-h)$ plane will degenerate to a single line, for both observations. We will therefore begin by determining this intersection point, which will pinpoint the values of H and h that belong to the true debris particle. We will use the STM derived in §3.2 as part of a predictor-corrector method in determining this intersection point.

One would have to be fairly lucky to by chance have discretized the initial $(\rho, \dot{\rho})$ plane so that $T(70;0)\{\mathcal{A}\}$ has a point *exactly* on the intersection in the (H, h) plane. If we were to zoom in on the intersection point in Fig. 4, we would be more likely to see something as in Fig. 5. Here the red points are the images of VD particles from the initial observation, projected onto the (H, h) plane, i.e. they are points from the set $T(70;0)\{\mathcal{A}\}$. Similarly, the black points are from the new observation, i.e. they are from the set $T(70;70)\{\mathcal{A}_{70}\}$. All of the points in Fig. 5 are actually coagulation points: their preimages on the $(\rho, \dot{\rho})$ plane are actually lines that run through the admissible region. Our goal is to determine *a single point* on the preimage. We will show how to generate the full curve from a single point in the next subsection.

For convenience we will use the coordinates $(\rho, \dot{\rho})$ as coordinates for the initial admissible region $\mathcal{C}$ belonging to the first observation and the coordinates $(\varrho, \dot{\varrho})$ as coordinates for the second admissible region $\mathcal{C}_{70}$ belonging to the second observation.

We begin by choosing an initial guess. We take one of the intersection point's neighboring points $\langle H_0, h_0 \rangle \in T(70;0)\{\mathcal{A}\}$, which is mapped from $\langle \rho, \dot{\rho} \rangle \in \mathcal{C}$. The

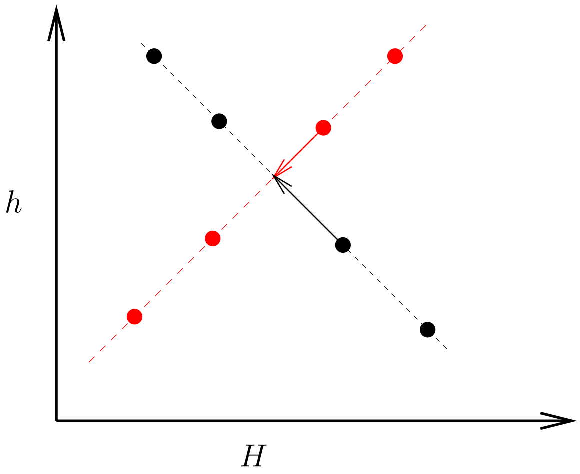

Figure 5: Example Schematic for Locating the Intersection Point on the $(H - h)$ Plane

partial STM tells us the effect of varying $\langle \rho, \dot{\rho} \rangle$ on the point $\langle H, h \rangle$, i.e. for the black points on Fig. 5:

$$\begin{bmatrix} \delta H_0 \\ \delta h_0 \end{bmatrix} = \mathbb{H}_0 \begin{bmatrix} \delta \rho \\ \delta \dot{\rho} \end{bmatrix}$$

Similarly for the second observation, we will consider the nearby point $\langle H_{70}, h_{70} \rangle$ which belongs to the point $\langle \varrho, \dot{\varrho} \rangle$ of the admissible region. Thus, for the red points on Fig. 5:

$$\begin{bmatrix} \delta H_{70} \\ \delta h_{70} \end{bmatrix} = \mathbb{H}_{70} \begin{bmatrix} \delta \varrho \\ \delta \dot{\varrho} \end{bmatrix}$$

So the game now is to find a set of points on both admissible regions, $\langle \delta\rho, \delta\dot{\rho} \rangle$ and $\langle \delta\varrho, \delta\dot{\varrho} \rangle$, so that their images under the mapping $T(70; 0)$ and $T(70; 70)$, respectively, lies on the intersection point. The condition is:

$$\begin{bmatrix} H_{70} \\ h_{70} \end{bmatrix} + \mathbb{H}_{70} \cdot \begin{bmatrix} \delta \varrho \\ \delta \dot{\varrho} \end{bmatrix} = \begin{bmatrix} H_0 \\ h_0 \end{bmatrix} + \mathbb{H}_0 \cdot \begin{bmatrix} \delta \rho \\ \delta \dot{\rho} \end{bmatrix}$$

This can be rearranged as follows:

$$\begin{bmatrix} \Delta H \\ \Delta h \end{bmatrix} := \begin{bmatrix} H_{70} - H_0 \\ h_{70} - h_0 \end{bmatrix} = \mathbb{H}_0 \cdot \begin{bmatrix} \delta \rho \\ \delta \dot{\rho} \end{bmatrix} - \mathbb{H}_{70} \cdot \begin{bmatrix} \delta \varrho \\ \delta \dot{\varrho} \end{bmatrix} \tag{20}$$

Since the image of the admissible region $\mathcal{A}$ under the transformation $T(t; t_0)$ is a line when projected onto the (H, h) plane, both state transition matrices $\mathbb{H}_0$ and $\mathbb{H}_{70}$ have a single zero eigenvector. Due to this degeneracy, there is no one unique predictor vector, which is all right because we are only looking for a single point in the admissible region that corresponds to the intersection point on the (H, h) plane. The easiest approach is to do the following. If $\langle 1, 0 \rangle^T \notin \text{null}(\mathbb{H}_0)$, we take $\delta\dot{\rho} = 0$; otherwise we take $\delta\rho = 0$. Additionally, if $\langle 1, 0\rangle^T \notin \text{null}(\mathbb{H}_{70})$, we take $\delta\dot{\varrho} = 0$; otherwise we take $\delta\varrho = 0$. For considerations here, we will assume both $\langle 1, 0\rangle^T \notin \text{null}(\mathbb{H}_0)$ and $\langle 1, 0\rangle^T \notin \text{null}(\mathbb{H}_{70})$, so that we can take $\delta\dot{\rho} = 0$ and $\delta\dot{\varrho} = 0$. If either of these conditions fails, the procedure presented here can be easily modified accordingly.

Begin by defining $\mathbf{z} = \langle \Delta H, \Delta h\rangle^T$. Let $\mathbf{h}_0$ and $\mathbf{h}_{70}$ be the first columns of the matrices $\mathbb{H}_0$ and $\mathbb{H}_{70}$, respectively. Let $\mathbf{h}_0^\perp$ and $\mathbf{h}_{70}^\perp$ be unit vectors perpendicular to the vectors $\mathbf{h}_0$ and $\mathbf{h}_{70}$, respectively. Then by prescribing the conditions $\delta\dot{\rho} = 0$ and $\delta\dot{\varrho} = 0$, (20) reduces to:

$$\mathbf{z} = (\delta\rho)\mathbf{h}_0 - (\delta\varrho)\mathbf{h}_{70}$$

Dotting this equation with $\mathbf{h}_{70}^\perp$ and solving for $\delta\rho$ we obtain:

$$\delta\rho = \frac{\mathbf{h}_{70}^\perp \cdot \mathbf{z}}{\mathbf{h}_{70}^\perp \cdot \mathbf{h}_0}$$

Similarly, by dotting with $\mathbf{h}_0^\perp$, we can obtain the following for $\delta\varrho$:

$$\delta\varrho = -\frac{\mathbf{h}_0^\perp \cdot \mathbf{z}}{\mathbf{h}_0^\perp \cdot \mathbf{h}_{70}}$$

This now gives us a new approximation for the intersection point. We reapply as necessary.

Both of the 2×2 $\mathbb{H}$-matrices will have a degeneracy in the form of a zero eigenvalue. The corresponding eigenvector we call the *zero eigenvector.* The zero eigenvector itself is *not* the zero vector, rather it is the eigenvector that corresponds to the zero eigenvalue, i.e. the vector that spans the null space of $\mathbb{H}$. $\mathbb{H}$ clearly has a zero eigenvector, if the initial observation is made at zenith, because the two-dimensional uncertainty region $\mathcal{C}$ on the $(\rho, \dot{\rho})$ plane reduces to a one-dimensional line on the (H, h) plane. Suppose $\xi(\rho, \dot{\rho})$ is the zero eigenvector of $\mathbb{H}$ at $(\rho, \dot{\rho}) \in \mathcal{C}$. The above algorithm provides a single point $(\rho^*, \dot{\rho}^*) \in \mathcal{C}$ that maps to the intersection point on the (H, h) plane. There exists a one-dimensional curve $\gamma(s) : (E \subset \mathbb{R}) \to \mathcal{C}$, such that $\gamma(0) = (\rho^*, \dot{\rho}^*)$, $\gamma(s) = (\rho(s), \dot{\rho}(s))$, and such that the projection onto the (H, h) plane of the image of γ under the mapping $T(70; 0)$ is the single intersection point of the two admissible curves on the (H, h) plane. The curve γ is then generated by the condition that $\gamma'(s) = \xi(\rho(s), \dot{\rho}(s))$, for all $s \in E$. So to generate a discretized sequence of points along γ, we integrate the zero-eigenvector of $\mathbb{H}$, starting from $(\rho^*, \dot{\rho}^*)$, until the curve exits the admissible region $\mathcal{C}$. In this way, once we determine a single point $(\rho^*, \dot{\rho}^*)$ on the admissible region $\mathcal{C}$ that corresponds to the intersection point in (H, h) space, a reduced admissible region $\mathcal{C}^r \subset \mathcal{C}$ can then be defined.

If the observation is made at zenith, we will have that $\dot{\rho} = \dot{r}$, i.e. the rate of change of the radial coordinate in the frame attached to the observation location will coincide with the rate of change of the radial coordinate in geocentric spherical coordinates. Since the debris particle's angular momentum is independent of $\dot{r}$, we find that the Delaunay variables G, H, and h will all be independent of $\dot{\rho}$. Because of this, zenith observations will have the property that $\mathbb{H}$ will have a constant zero eigenvector of

$\langle 0, 1\rangle$, throughout the admissible region $\mathcal{C}$. As a consequence of the above theorem, the reduced admissible region will be the intersection of the vertical line $\rho = \rho^*$ with the admissible region $\mathcal{C}$. We call the reduced admissible region $\mathcal{C}^r$ and likewise define

$$\mathcal{A}^r := \{\langle \rho, \dot{\rho}, \alpha, \delta, \dot{\alpha}, \dot{\delta}\rangle : (\alpha, \delta, \dot{\alpha}, \dot{\delta}) = A \text{ and } (\rho, \dot{\rho}) \in \mathcal{C}^r\}$$

to be the (one dimensional) admissible region of the observation space. By construction, the projection of $T(t; t_0)\{\mathcal{A}^r\}$ on the (H, h) plane will correspond to a single point: the intersection point as seen in Fig. 4 and Fig. 5. A similar statement can be made about $\mathcal{C}_{70}$ and $\mathcal{A}_{70}$, which are defined analagously for the second observation.

The reduced admissible regions $\mathcal{C}^r$ and $\mathcal{C}^r$ for the initial and second observation are plotted in Fig. 6. Their images under the transformation T, projected onto each of the three Delaunay planes, is shown in Fig. 7.

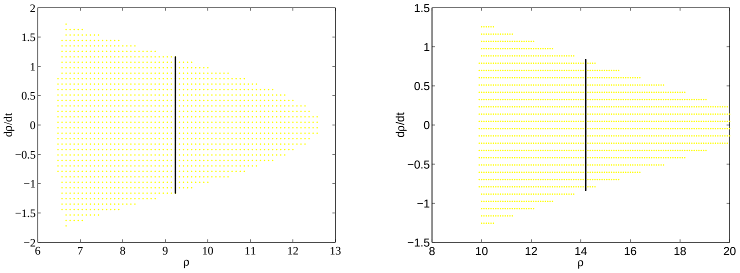

Figure 6: $\mathcal{C}$ (yellow) with $\mathcal{C}^r$ (black), left; $\mathcal{C}_{70}$ (yellow) with $\mathcal{C}_{70}^r$ (black), right

5.3 Orbit Determination

By reducing the admissible regions $\mathcal{C}$ and $\mathcal{C}_{70}$ to the preimage of the intersection point on the (H, h) Delaunay plane, we found that the dimensionality of the admissible region can be reduced from 2 to 1. One can see that an additional reduction can be made by considering the projection of these curves on the (L, l) Delaunay plane, as seen in Fig. 7. These curves have five distinct intersection points on the (L, l) plane, therefore the actual uncertainty distribution has been reduced from a two-dimensional sheet to that of five distinct points in phase space. Additional information is also available from the overlap region of the two reduced curves as projected onto the (G, g) plane. In the case we are considering, only one of the five intersection points on the (L, l) plane actually lines up as an intersection point on the (G, g) plane. Therefore, the orbit is determined uniquely.

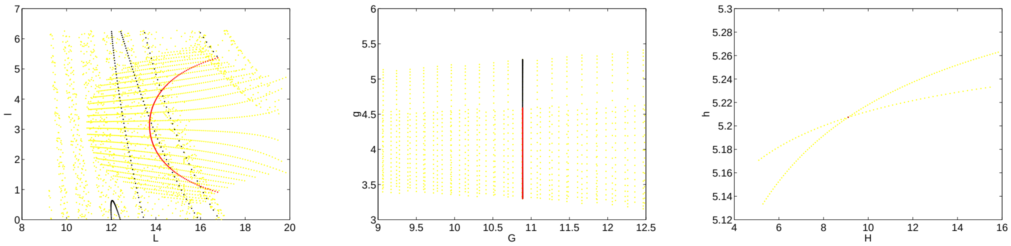

Figure 7: Fig. 4 plots (yellow) with $T(70;0)\{\mathcal{A}^r\}$ (red) and $T(70;70)\{\mathcal{A}^r_{70}\}$ (black)

6 Orbit Determination II: Kepler Orbit with 2 Near-Zenith Observations

In this section we will study the case of two near-zenith observations. If the observation is not made when the space debris particle is directly overhead, the projection of the uncertainty region on the (H, h) plane will no longer be one-dimensional. We will consider the same 2 attributable vectors that were observed in §5, but nudge the inertial location of the observer so that the observations do not correspond to zenith observations. The first attributable vector is given by $A = (0, \pi/6, 0.1, 0.03)$, made at time $t = 0$ from a point on the Earth's surface $\Theta = \pi/3+0.1$, $\Phi = 0.1$. Assuming particle #1000 is the true space debris particle, a possible second observation (nonzenith) might be given by the attributable vector $A_{70} = (1.1516, 0.4790, 0.2262, -0.0809)$, made at time $t = 70$ from a point on the Earth's surface $\Theta = 1.2516$, $\Phi = 1.1918$. The intersections of the admissible regions, as projected onto the Delaunay planes, is shown in Fig. 8. Because the true debris particle did not fly directly over zenith on either of the measurements, the admissible regions now have two-dimensional projections on the (H, h) plane. Since we are considering the Kepler case, the original uncertainty distribution's projections on the (G, g) and (H, h) plane are static. Our goal now is to systematically reduce the uncertainty region, by considering each Delaunay plane in sequence, as much as possible until it is reduced to either a single

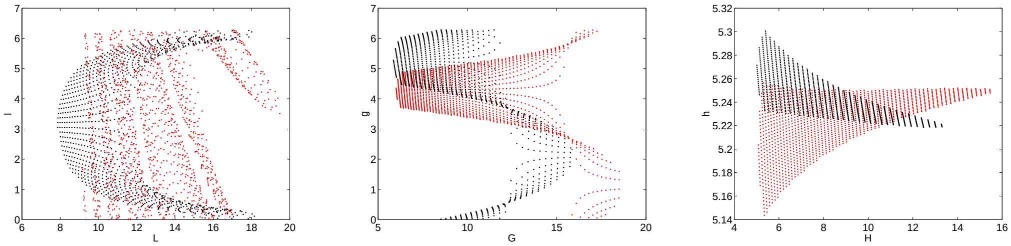

Figure 8: $T(70;0)\{\mathcal{A}\}$ (red) and $T(70;70)\{\mathcal{A}_{70}\}$ (black) projected onto the Delaunay planes, nonzenith observations

point (complete orbit determination) or a one-dimensional line.

By examination of the concurrent Delaunay plots of the uncertainty region projections (Fig. 8), we choose to begin the orbit determination process by cutting off the non-overlap sections of the surface in the (H, h) plane. The Delaunay projections of the remaining piece of surface is shown in Fig. 9. We see in Fig. 9 that there is again

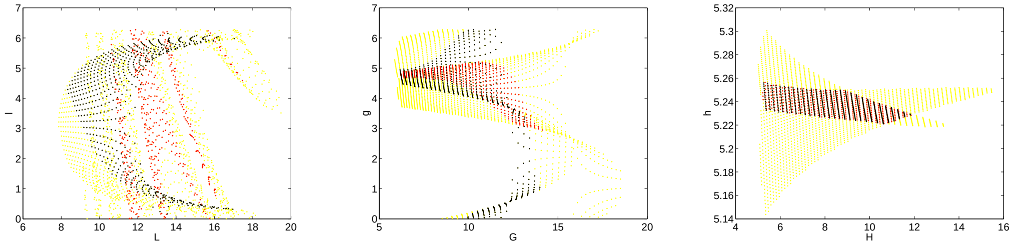

Figure 9: $T(70;0)\{\mathcal{A}^r\}$ (red) and $T(70;70)\{\mathcal{A}^r_{70}\}$ (black) projected onto the Delaunay planes, nonzenith observations

an overlap and non-overlap region in the (G, g) plane. Removing the non-overlap region further reduces the admissible region, as shown in Fig. 10. Interestingly, the

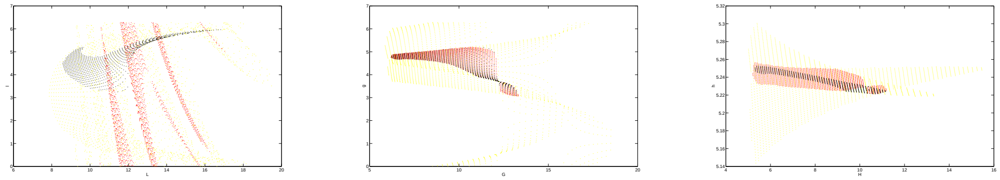

Figure 10: $T(70;0)\{\mathcal{A}^{rr}\}$ (red) and $T(70;70)\{\mathcal{A}^{rr}_{70}\}$ (black) projected onto the Delaunay planes, nonzenith observations

(H, h) projection can be again used to cut out more of the uncertainty surface, resulting in a third reduction, as shown in Fig. 11. We now turn to the projection of

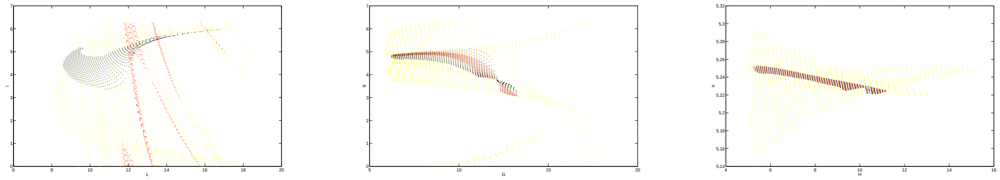

Figure 11: $T(70;0)\{\mathcal{A}^{rrr}\}$ (red) and $T(70;70)\{\mathcal{A}^{rrr}_{70}\}$ (black) projected onto the Delaunay planes, nonzenith observations

the thrice reduced uncertainty region on the (L, l) plane. The first three reductions have eliminated all but three overlap regions on the (L, l) plane. We consider each in term. The systematic projection of each overlap region onto each of the three Delaunay planes is shown in Fig. 12. We see that the far right overlap region on the

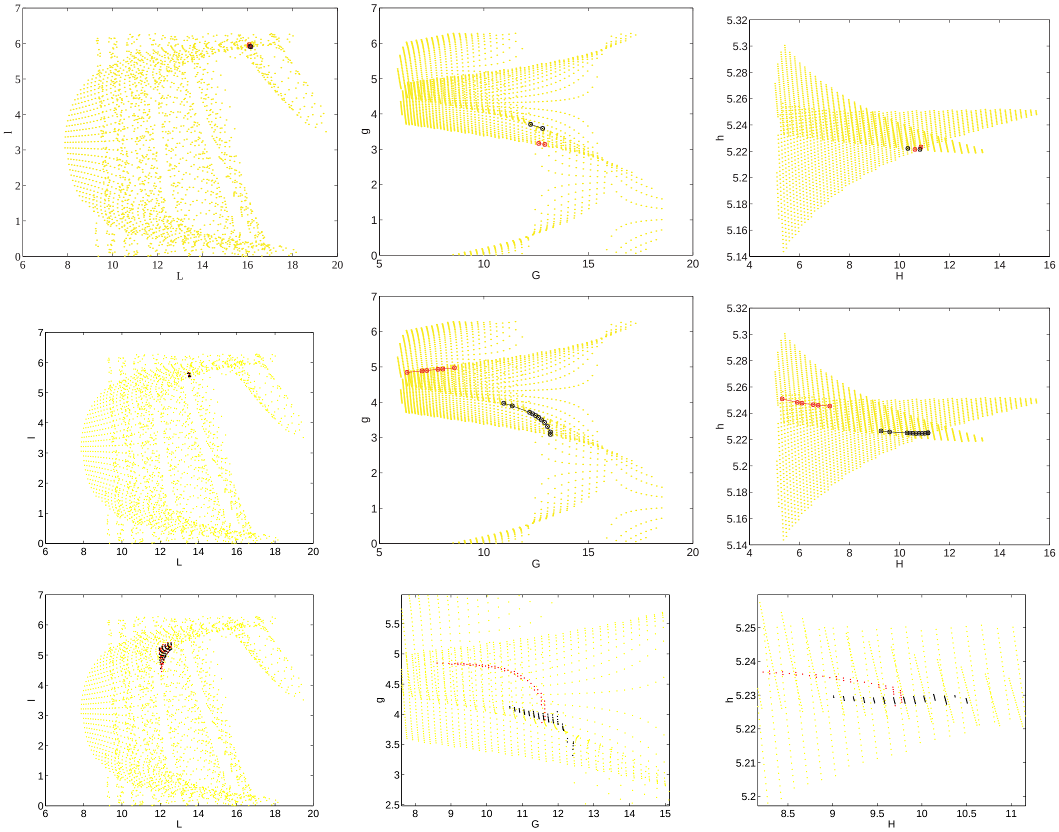

Figure 12: $T(70; 0)\{\mathcal{A}^{rrrr}\}$ (red) and $T(70; 70)\{\mathcal{A}^{rrrr}_{70}\}$ (black) projected onto the Delaunay planes, nonzenith observations

(L, l) plane (the overlap that is almost confined to a single point) does not overlap on the (G, g) plane. This overlap region thus cannot correspond to the actual debris particle and is now ruled out. The middle overlap region on the (L, l) plane does not overlap on the (G, g) or (H, h) plane, so it is ruled out. Finally, the leftmost overlap region has a small intersection on both the (G, g) and (H, h) plane. The orbit is thus determined to within a small uncertainty about a single point in Delaunay space. It is possible that further reductions can be made by continuing this process: cut away the nonoverlap region of the (G, g) plane, then do the same for the new nonoverlap region of the (H, h) plane, and continue to ping-pong back and forth until the intersection is known to within the desired uncertainty. Alternatively, since the actual orbit is now known to within a small neighborhood of a single point, a least squares solution can be carried out.

7 Orbit Determination III: J_2 Orbit

The intersection of two admissible regions (eg. Fig. 4) can take on a variety of different appearances. The purpose of this section is twofold. The main purpose is to present the reader with a menagerie of qualitatively different examples to give the reader a broader feel for how these overlap regions can appear. We will do this in the context of the J_2 problem, so that we can also show how the case where one treats perturbations differs from the associated Kepler problem.

7.1 Dynamics of the J_2 Orbit

It is known that the gravitational potential of an axisymmetric body can be expanded in a series of the form:

$$V = -\frac{GM}{r}\left(1 - \sum_{n=2}^{\infty} \frac{J_n P_n(\cos(\theta))}{r^n}\right)$$

where θ is measured from the axis of symmetry, and $P_n(x)$ is the n-th Legendre polynomial. Taking into account the first order correction of the gravitational field of the Earth, due to its oblateness, the potential can be approximated by the potential:

$$V \approx -\frac{\mu}{r} + \frac{\mu J_2(3\cos^2\theta - 1)}{r^2}$$

where μ is the gravitational parameter of the Earth and $J_2 \approx 1.08 \times 10^{-3}$ is the Earth's J_2 term. The disturbing function for the averaged potential for the J_2 problem can be written as (Danby [7]):

$$R = \frac{\mu J_2}{2a^2(1-e^2)^{3/2}}\left(\frac{3}{2}\sin^2 i - 1\right)$$

The full Hamiltonian for the averaged J_2 problem can be written as:

$$\mathcal{H} = -\frac{\mu}{2a} + \frac{\mu J_2}{2a^2(1-e^2)^{3/2}}\left(\frac{3}{2}\sin^2 i - 1\right)$$

Substituting the orbit elements with Delaunay variables (14), we can rewrite the potential as follows:

$$\mathcal{F} = -\frac{\mu^2}{2L^2} + \frac{\mu^4 J_2}{2L^3G^3}\left(\frac{1}{2} - \frac{3H^2}{2G^2}\right) \tag{21}$$

Applying Hamilton's equations (16) to the J_2 Hamiltonian (21), we obtain the following dynamic equations of motion for a particle in the Earth's J_2 field:

$$\begin{aligned}
\frac{dl}{dt} &= \frac{\mu^2}{L^3} - \frac{3\mu^4 J_2}{2L^4G^3}\left(\frac{1}{2} - \frac{3H^2}{2G^2}\right) \\
\frac{dg}{dt} &= \frac{15\mu^4 J_2 H^2}{4L^3G^6} - \frac{3\mu^4 J_2}{4L^3G^4} \\
\frac{dh}{dt} &= -\frac{3\mu^4 J_2 H}{2L^3G^5}
\end{aligned} \tag{22}$$

The conjugate momenta are conserved:

$$\frac{dL}{dt} = 0 \qquad \frac{dG}{dt} = 0 \qquad \frac{dH}{dt} = 0$$

7.2 STM of the J_2 Dynamics

The STM corresponding to the transformation $T_4(t;t_0)$ will no longer be given by (19). The solution to the dynamic equations of motion (22) for the J_2 problem are simply:

$$L(t) = L_0, \qquad G(t) = G_0, \qquad H(t) = H_0$$

$$l(t) = l_0 + \Lambda \cdot (t - t_0), \qquad g(t) = g_0 + \Gamma \cdot (t - t_0), \qquad h(t) = h_0 + \Xi \cdot (t - t_0)$$

where we define

$$\begin{aligned}
\Lambda &= \frac{\mu^2}{L^3} - \frac{3\mu^4 J_2}{2L^4 G^3}\left(\frac{1}{2} - \frac{3H^2}{2G^2}\right) \\
\Gamma &= \frac{15\mu^4 J_2 H^2}{4L^3 G^6} - \frac{3\mu^4 J_2}{4L^3 G^4} \\
\Xi &= -\frac{3\mu^4 J_2 H}{2L^3 G^5}
\end{aligned}$$

so that the STM is given by:

$$\Phi_4^{J_2}(t;t_0) = \begin{bmatrix}
1 & 0 & 0 & 0 & 0 & 0 \\
\Lambda_L(t-t_0) & 1 & \Lambda_G(t-t_0) & 0 & \Lambda_H(t-t_0) & 0 \\
0 & 0 & 1 & 0 & 0 & 0 \\
\Gamma_L(t-t_0) & 0 & \Gamma_G(t-t_0) & 1 & \Gamma_H(t-t_0) & 0 \\
0 & 0 & 0 & 0 & 1 & 0 \\
\Xi_L(t-t_0) & 0 & \Xi_G(t-t_0) & 0 & \Xi_H(t-t_0) & 1
\end{bmatrix}$$

where Λ_L, Λ_G, and Λ_H are the partial derivatives of $\Lambda(L, G, H)$ with respect to L, G, and H, respectively; and similarly for Γ and Ξ.

7.3 Concurrent Plot of 2 Zenith Observations on the Delaunay Planes

In this section we will assume the same initial observation of the debris particle as considered in §5, i.e. the attributable vector $A = (0, \pi/6, 0.1, 0.03)$ is recorded at $t = 0$ from the point $\Theta = \pi/3$, $\Phi = 0$, on the Earth's surface. The projections of the corresponding admissible region on the Delaunay planes are shown in Fig. 2. Taking into account the J_2 perturbation due to the Earth's oblateness on the debris particle's orbit, the time-evolved Delaunay projections are shown in Fig. 13. (The time-evolved Delaunay projections of the same admissible region in the Kepler case were shown in Fig. 3). One sees that at these time scales, the J_2 effect on the (L, l) and (G, g) planes

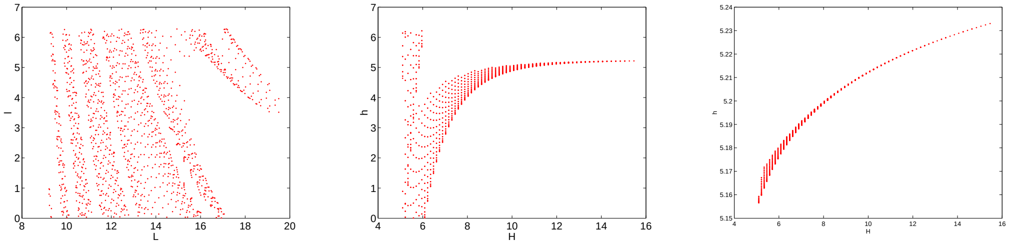

Figure 13: $T(70;0)\{\mathcal{A}\}$ projected onto the Delaunay planes, J_2 problem

is fairly insignificant. On the (H,h) plane, the J_2 perturbation causes the projection of the uncertainty surface to widen from a line to a narrow two-dimensional region, thus regenerating the degenerate surface projection.

We consider now the three cases that the actual debris particle is virtual debris particle #400, #600, and #1000. Assuming a second zenith observation of the debris particle is made after 70 hours, the two concurrent admissible region projections will appear as in Fig. 14. On the other hand, if the second observation is instead made after 140 hours, the concurrent projections of the two admissible regions will appear as in Fig. 15. Each of these 6 cases assume the same initial attributable vector with admissible region Fig. 13. Notice that the projection of $T(t;0)\{A\}$ on the (L,l) plane becomes more shredded as it dynamically evolves. In fact, modulo the perturbations, most of the dynamical evolution of the original uncertainty surface is contained within this shredding. We show these cases to give the reader a broader feel of the variety in which these uncertainty intersections can appear. Since we treat the intersection procedure in §5 and §6, we will not discuss it again here.

8 A Conceptual Algorithm

The purpose of this paper has been to introduce and illustrate the viability of this orbit determination technique. As such, all surface intersection reductions were carried out by hand. Future research must be done on the development of technology that efficiently automates this process. As intersections of two-dimensional surfaces must be performed, and not higher-dimensional surfaces, it is feasible to develop computationally efficient approaches for this. In this section we discuss an algorithm and indicate how one might use this technology in the orbit determination process and the subsequent inclusion of these new orbits in the space debris catalog when faced with a large number of observations per night. As was mentioned in §2.1, each observation should be recorded as an observation vector:

$$x = (A, t, L) \in \mathbb{R}^5 \times \mathbb{N}$$

containing an attributable vector, the observation time, and the observatory's location. Each new observation should be checked against the catalog of known objects.

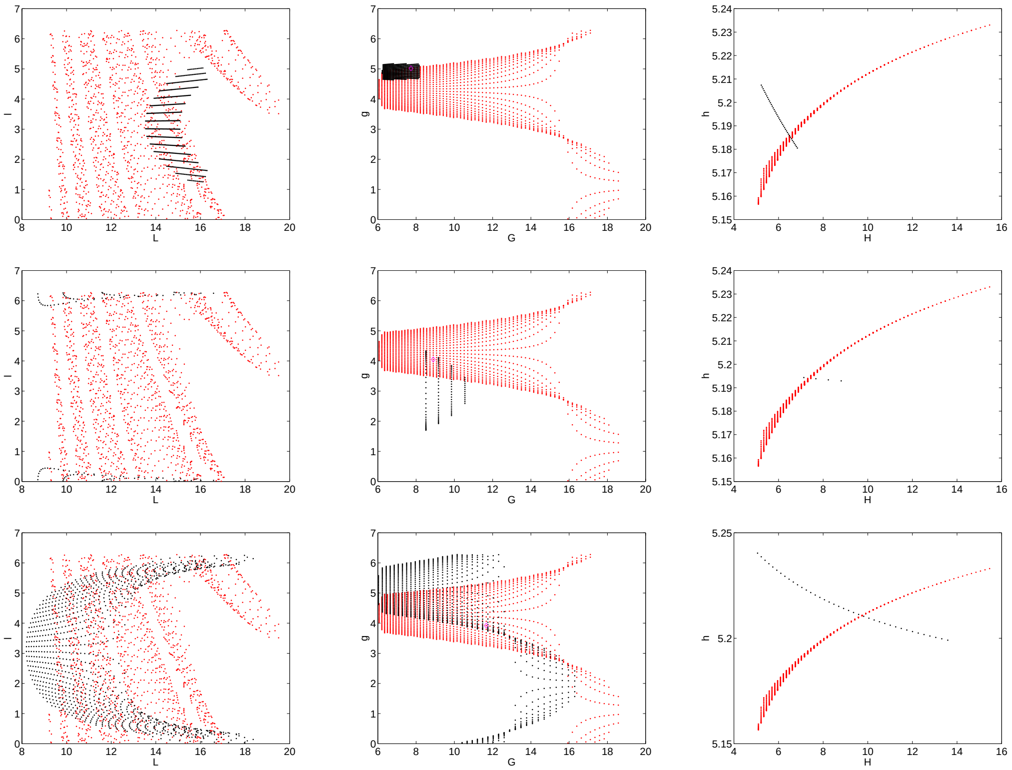

Figure 14: $T(70;0)\{\mathcal{A}\}$ (red) and $T(70;70)\{\mathcal{A}_{70}\}$ (black) projected onto the Delaunay planes, J_2 problem. Assumes the true particle is number #400, #600, and #1000, from top down.

If the observed attributable vector does not match any of the orbital particles in the catalog, it will be saved as an uncorrelated observation. A rolling observation window can be defined (for instance, one week) within which it is compared to all other uncorrelated observations. For these comparisons, a standard epoch time can be defined and all uncorrelated observations made within the observation window can then be mapped into the Delaunay planes and then dynamically evolved or regressed to the epoch time. These uncertainty projections can then be stored and intersected with all other such observations to discover which observations are correlated. For each orbit correlation that is found, the corresponding observations can then be saved in a secondary catalog, which is a temporary holding catalog, until the orbit is confirmed, at which time the data can be promoted to the primary catalog of correlated data.

9 Alternative Approaches

As we discussed in §4.2, the correlation and orbit determination between two data tracks is tantamount to finding the unique intersection point $\mathbf{\Delta}^*$ of two two-dimensional

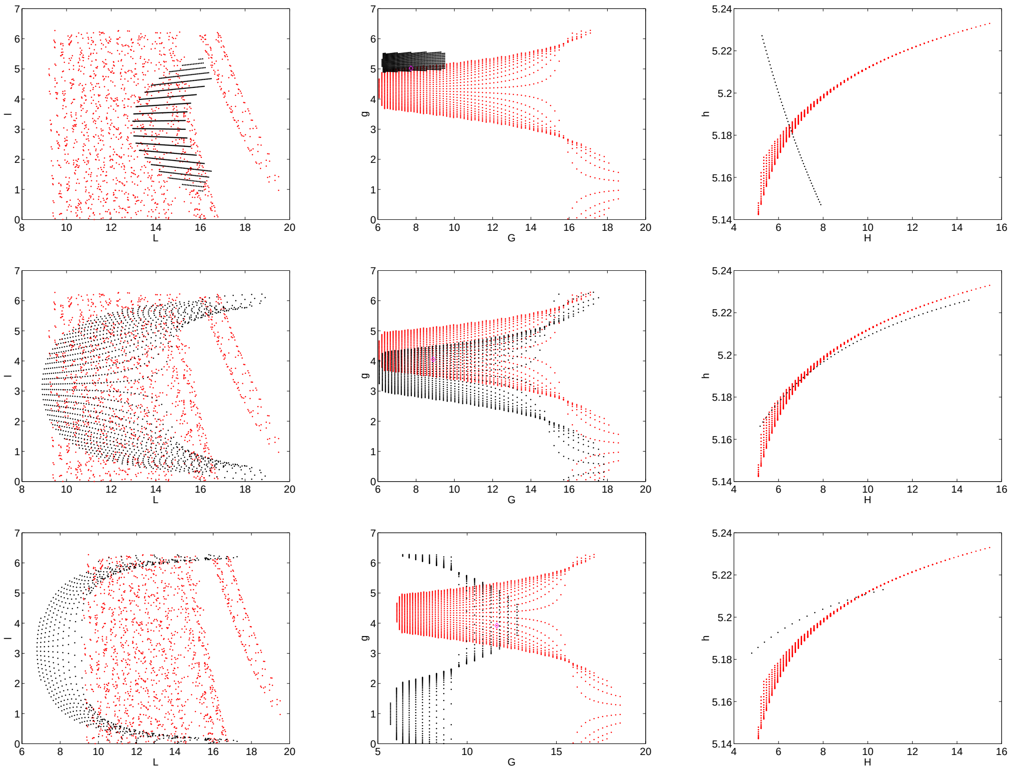

Figure 15: $T(140;0)\{\mathcal{A}\}$ (red) and $T(140;140)\{\mathcal{A}_{70}\}$ (black) projected onto the Delaunay planes, J_2 problem. Assumes the true particle is number #400, #600, and #1000, from top down.

submanifolds, $F^{\tau}_{\mathfrak{X}_1}(\mathcal{C}_1)$ and $F^{\tau}_{\mathfrak{X}_2}(\mathcal{C}_2)$, of six-dimensional Delaunay space $\mathcal{D} \cong \mathbb{R}^6$. It is the scope of this paper to discuss the feasibility of an approach, presented in this current work, known as Intersection Theory Analysis (ITA). The ITA algorithm was introduced in §4.3 and further illustrated by means of example in §5, 6, and 7, for the cases of zenith observations, non-zenith observations, and J_2 orbital perturbations, respectively. In this current section we will discuss some viable alternative approaches for determining the intersection point $\mathbf{\Delta}^*$, thus obtaining an orbit determination. A thorough analysis of these alternative approaches will be the study of future research; it is our goal here only to demonstrate the voracity of a subvolume intersection approach to orbit determination problems, in the sense that there are competing methodologies within this approach, each with its own merits, that could lead to fruitful results.

9.1 TITA

In this paper, we choose the Delaunay space to carry out the ITA process for several reasons. As opposed to orbital element space, the Delaunay space is a symplectic space. This characteristic is beneficial for two reasons. The symplecticity of this space brings with it added structure and geometric invariants that may prove useful in understanding the resulting dynamics. But moreover, on a more mundane but simultaneously more practical level, there is a natural pairing of coordinates, yielding a natural fracture of the space into three separate two-dimensional projective spaces, in which intersections are more effictively carried out. Since the true space is a splicing of these individual projective spaces, the intersection process can be repeated until a single intersection point emerges as victor. The other benefit of using Delaunay coordinates is that it provides a standard space for comparison of competing uncertainty manifolds. For each observation window (e.g. perhaps a rolling two week time span), a common epoch time is defined and all uncertainty manifolds are mapped to the Delaunay space and then dynamically evolved or regressed to that epoch time. These uncertainty manifolds can therefore be pairwise compared in this common space.

As an alternative, one can perform TITA - topocentric Intersection Theory Analysis. As the name suggests, TITA involves performing the same Intersection Theory Analysis routine in the topocentric observation geometry as opposed to the Delaunay space. As the topocentric viewing geometry is continuously transforming, there is no common space in which to compare all uncertainty distributions. Instead, for each pair of tracks, one does the following. First compute the admissible region corresponding to each track of data. Pull the second admissible regions back into geocentric cartesian coordinates, dynamically map the resulting distribution forward or backward in time to the time of the first track, then push the resulting manifold forward to the topocentric coordinates in which the first track was viewed. This approach has the possible disadvantage that *for each pair* of tracks, an uncertainty surface must be mapped into a new space, entailing a total of $O(N^2)$ surface mappings for a set of N uncorrelated tracks. Recall that for regular ITA, each uncertainty surface is *mapped once* into a common space for comparison, yielding a total of $O(N)$ such mappings. In the TITA approach, one then carries out the ITA algorithm in the topocentric observation projective spaces $\mathcal{O}_\rho = (\rho, \dot{\rho})$, $\mathcal{O}_\alpha = (\alpha, \dot{\alpha})$, and $\mathcal{O}_\delta = (\delta, \dot{\delta})$. TITA has the advantage that, when performing ITA in the observation projective spaces, that *one* of the uncertainty surfaces degenerates to *a single point* in the projective spaces $\mathcal{O}_\alpha$ and $\mathcal{O}_\delta$. Thus, ITA degenerates to checking to see if the second uncertainty manifold contains in it a four-vector $\vec{\theta} = \langle \alpha, \dot{\alpha}, \delta, \dot{\delta} \rangle$ in an epsilon-neighborhood of the original attributable vector A of the first observation. If so, one then checks if the corresponding $\langle \rho, \dot{\rho} \rangle$ of the second uncertainty surface lie on the admissible region of the first. Thus the ease with which one performs ITA in the topocentric projective space and added computation associated with the additional surface mappings must be compared with the relative complexity in performing intersections in the Delaunay projective spaces and the associated computational advantage of performing fewer surface mappings.

9.2 Metric Approaches

As the ultimate goal is to find the intersection point shared by two two-dimensional surfaces $F^{\mathcal{T}}_{\mathfrak{X}_1}(\mathcal{C}_1)$ and $F^{\mathcal{T}}_{\mathfrak{X}_2}(\mathcal{C}_2)$, each represented by a discretized VD field mapped to Delaunay space, a natural approach might be to find the pair of points $\mathbf{\Delta}^*_1 \in F^{\mathcal{T}}_{\mathfrak{X}_1}(\mathcal{C}_1)$ and $\mathbf{\Delta}^*_2 \in F^{\mathcal{T}}_{\mathfrak{X}_2}(\mathcal{C}_2)$ which are "closest together" in some sense. The accomplishment of this objective depends on the suitable choice of a metric for the Delaunay space $\mathcal{D}$. Taking the example of two zenith-observations considered in §5, there are literally hundreds of point pairs, $\{\mathbf{\Delta}_{1i} \in F^{\mathcal{T}}_{\mathfrak{X}_1}(\mathcal{C}_1); \mathbf{\Delta}_{2i} \in F^{\mathcal{T}}_{\mathfrak{X}_2}(\mathcal{C}_2)\}_{i=1}^{100's}$, whose Euclidean separation distance $||\mathbf{\Delta}_{1i} - \mathbf{\Delta}_{2i}||_{\text{Euclid}}$ is less than the distance between the actual approximate intersection points $\mathbf{\Delta}^*_1$ and $\mathbf{\Delta}^*_2$ yielded by ITA and known to be correct by construction. Many of these false positives don't even hit the obvious intersection point on the (H, h) plane (see Fig. 4). Clearly a much more judicious choice of metric is needed. One could imagine that with the correct metric, the pair of points that lies closest together will always be the intersection point. Such a discovery would greatly reduce the computational complexity of repeatedly performing successive intersections between overlapping planar laminas.

Typically when one speaks of a metric one thinks of it as being defined globally, i.e. we would have:

$$\mathbf{g} : T\mathcal{D} \times T\mathcal{D} \to \mathbb{R}$$

We will, however, require a metric, $\mathbf{g}_1$, that is defined only on the restriction of $\mathcal{D}$ to the submanifold $F^{\mathcal{T}}_{\mathfrak{X}_1}(\mathcal{C}_1)$, so that:

$$\mathbf{g}_1 : T\mathcal{D}|_{F^{\mathcal{T}}_{\mathfrak{X}_1}(\mathcal{C}_1)} \times T\mathcal{D}|_{F^{\mathcal{T}}_{\mathfrak{X}_1}(\mathcal{C}_1)} \to \mathbb{R}$$

Note $\mathbf{g}_1$ takes as inputs full six-dimensional vectors from $T\mathcal{D}$, only it is defined solely at points located on the submanifold $F^{\mathcal{T}}_{\mathfrak{X}_1}(\mathcal{C}_1)$; it is *not* the tangent bundle to this submanifold. For any point $\mathbf{\Delta}_1 \in F^{\mathcal{T}}_{\mathfrak{X}_1}(\mathcal{C}_1)$, the metric $\mathbf{g}_1(\mathbf{\Delta}_1)$ is a good approximation for the metric in a local neighborhood $\mathcal{U} \subset \mathcal{D}$ of $\mathbf{\Delta}_1$. Thus for any $\mathbf{\Delta} \in \mathcal{U}$, the distance between $\mathbf{\Delta}$ and $\mathbf{\Delta}_1$ is approximated by

$$d(\mathbf{\Delta}, \mathbf{\Delta}_1) \approx \sqrt{(\mathbf{\Delta} - \mathbf{\Delta}_1)^T \cdot \mathbf{g}_1(\mathbf{\Delta}_1) \cdot (\mathbf{\Delta} - \mathbf{\Delta}_1)}$$

However if the point $\mathbf{\Delta}$ is far away, we care less about the actual measure of this distance than about the fact that it is far away. Hence one can simply seek the points $\mathbf{\Delta}^*_1$ and $\mathbf{\Delta}^*_2$ that minimize

$$D_{\min} = \inf_{\mathbf{\Delta}_1 \in F^{\mathcal{T}}_{\mathfrak{X}_1}(\mathcal{C}_1)} \left[\inf_{\mathbf{\Delta}_2 \in F^{\mathcal{T}}_{\mathfrak{X}_2}(\mathcal{C}_2)} \left(\sqrt{(\mathbf{\Delta}_2 - \mathbf{\Delta}_1)^T \cdot \mathbf{g}_1(\mathbf{\Delta}_1) \cdot (\mathbf{\Delta}_2 - \mathbf{\Delta}_1)} \right) \right]$$

Since both submanifolds are discretized by VD fields, one simply compares this quantity for pairwise sets of points.

As mentioned above, the successful actualization of this method depends on the correct choice of metric $\mathbf{g}_1$. Such a metric might be constructed as to preserve the integrity and structure of the observation geometry in which the attributable vector was first recorded. The Euclidean metric induces the following metric on the spherical coordinates $\langle \rho, \dot{\rho}, \alpha, \delta, \dot{\alpha}, \dot{\delta} \rangle$ used in the topocentric (TC) frame:

$$\mathbf{g}_{\mathrm{TC}} = \begin{pmatrix} 1 & 0 & 0 & 0 & 0 & 0 \\ 0 & 1 & 0 & 0 & 0 & 0 \\ 0 & 0 & \rho\cos\delta & 0 & 0 & 0 \\ 0 & 0 & 0 & \rho & 0 & 0 \\ 0 & 0 & 0 & 0 & \rho\cos\delta & 0 \\ 0 & 0 & 0 & 0 & 0 & \rho \end{pmatrix}$$

One can simply push this metric forward to Delaunay space in the following sense. For any $\boldsymbol{\Delta} \in F^{\tau}_{\mathfrak{X}_1}(\mathcal{C}_1)$ and $\mathbf{v}_1,\ \mathbf{v}_2 \in T_{\boldsymbol{\Delta}}\mathcal{D}$, define

$$\mathbf{g}_1(\boldsymbol{\Delta})(\mathbf{v}_1, \mathbf{v}_2) = \mathbf{g}_{\mathrm{TC}}(F^{\tau}_{\mathfrak{X}_1}{}^{-1}(\boldsymbol{\Delta}))\left((dF^{\tau}_{\mathfrak{X}_1})^{-1} \cdot \mathbf{v}_1, (dF^{\tau}_{\mathfrak{X}_1})^{-1} \cdot \mathbf{v}_2\right)$$

Since the matrix of the linear transformation $dF^{\tau}_{\mathfrak{X}_1}$ is simply the Jacobian matrix Φ of the transformation, computation of which was discussed in §3.2, which is easily computed, we have:

$$\mathbf{g}_1(\boldsymbol{\Delta})(\mathbf{v}_1, \mathbf{v}_2) = \mathbf{g}_{\mathrm{TC}}(F^{\tau}_{\mathfrak{X}_1}{}^{-1}(\boldsymbol{\Delta}))\left(\Phi^{-1} \cdot \mathbf{v}_1, \Phi^{-1} \cdot \mathbf{v}_2\right) = \mathbf{v}_1^T \cdot (\Phi^{-1})^T \cdot \mathbf{g}_{\mathrm{TC}} \cdot \Phi^{-1} \cdot \mathbf{v}_2$$

we have the matrix of the metric $\mathbf{g}_1$ is given by:

$$\mathbf{g}_1 = (\Phi^{-1})^T \cdot \mathbf{g}_{\mathrm{TC}} \cdot \Phi^{-1}$$

This approach is not as of yet entirely robust, as it still returns false positives for the intersection point. However, it seems to preserve the visual sense of closeness one has from visual examination of the Delaunay planes, i.e. points close together actually look close together. This has not always been the case with other metrics we experimented with. Further investigation and development of this metric will be a topic of future research.

10 Conclusion

In this paper, we presented a method for the orbit determination of two previously uncorelated observations of space debris particles. We considered the case of a Kepler orbit with two zenith measurements, the case of a Kepler orbit with two non-zenith measurements, and also the case where the J_2 perturbation was included. Each observation is to be treated as a two-dimensional uncertainty surface, and can be mapped into the symplectic Delaunay space. For the unperturbed problem the projections of this surface onto the (G, g) and (H, h) Delaunay planes are static, and the projection on the (L, l) plane shifts at a rate dependent upon only (L). The Delaunay space is actually the action-angle space, and is isomorphic to $T^3 \times \mathbb{R}^3 = S^1 \times S^1 \times S^1 \times \mathbb{R}^3$.

Since the angles $l,\ g,\ h$ are modulo 2π, and each $L = const.$ strip of the (L, l) projection of the uncertainty surface progresses along at a constant rate in time, the surface projection on the (L, l) plane becomes more and more "shredded" as time evolves. Since the other two symplectic projections of the surface are static for the Kepler problem, this shredding occurs *without* an increase or decrease to the total projected area on the (L, l) plane. In order to correlate two separate observations, their respective uncertainty surfaces are to be mapped to the same epoch time and then projected concurrently onto the three Delaunay planes. If both observations are zenith observations, the projections of these surfaces onto the (H, h) plane degenerate to a single line and a unique orbit determination can be made as outlined in 5. This orbit determination process is robust as a similar process can be used to determine the orbit in the case of two nonzenith observations, as we showed in §6. Our goal in the present work has been to present a qualitative overview of this process and indicate the existence and robustness of this process. Future work is needed in the development of an efficient algorithm that will automate the uncertainty reduction process we illustrated here. Furthermore, uncertainty in the attributable vector must also be taken into account. This too will be the topic of future work.

References

[1] Abraham, R. and Marsden, J.E., "Foundations of Mechanics," 2nd ed., Addison-Wesley, 1978.

[2] Arnold, V.I., "Mathematical Methods of Classical Mechanics, 2nd Ed.," Springer-Verlag, 1978.

[3] Born, M., "The Mechanics of the Atom," G. Bells and Sons, Ltd, London, 1927.

[4] Brouwer, D. and Celemence, G.M., "Methods of Celestial Mechanics," Acedemic Press, 1961.

[5] Chang, D.E. and Marsden, J.E., Geometric Derivation of the Delaunay Variables and Geometric Phases, Celestiam Mechanics and Dynamical Astronomy, 86: 185-208, 2003.

[6] Crassidis, J.L. and Junkins, J.L., "Optimal Estimation of Dynamic Systems," Chapman & Hall/CRC, 2004.

[7] Danby, J.M.A., "Fundamentals of Celestial Mechanics," Willmann-Bell, 1988.

[8] Delaunay, C., Theorie du mouvement de la lune, in "Memoires de l'Academie des Sciences," vol. 28, 1860.

[9] Delaunay, C., Theorie du mouvement de la lune, in "Memoires de l'Academie des Sciences," vol. 29, 1867.

[10] Ferraz-Mello, S., "Canonical Perturbation Theories: Degenerate Systems and Resonance," Springer, 2007.

[11] Greenwood, D.T., "Classical Dynamics," Dover, 1997, pp. 182–183.

[12] T.W. Hamilton and W.G. Melbourne. 1966. "Information Content of a Single Pass of Doppler Data from a Distant Spacecraft," *JPL Space Programs Summary*, Vol. 3, No. 37 - 39, 1966, pp. 18 - 23.

[13] Marsden, J.E. and Ratiu, T.S., "Introduction to Mechanics and Symmetry, 2nd Ed.," Springer, 1999.

[14] Maruskin, J.M., Scheeres, D.J., and Bloch, A.M., "Dynamics of Symplectic Sub-Volumes," To be published in the Proceedings of the 2007 IEEE Conference on Decision and Control.

[15] Maruskin, J.M., Scheeres, D.J., and Bloch, A.M., "Dynamics of Symplectic Sub-Volumes," submitted to the SIAM Journal of Applied Dynamical Systems, 2007.

[16] J.M. Maruskin, D.J. Scheeres and A.M. Bloch. "SubVolumes in Dynamical Systems and the Tracking of Space Debris," paper presented at the 2007 AAS/AIAA Astrodynamics Specialist Conference, Mackinac Island, Michigan, August 19-23, 2007. AAS 07 - 392

[17] A. Milani, G. Gronchi, M. Vitturi, and Z. Knezevic. 2004. "Orbit Determination with Very Short Arcs. I Admissible Regions," *Celestial Mechanics and Dynamical Astronomy* 90: 57-85.

[18] J. Virtanen and K. Muinonen. 2001. "Statistical Ranging of Asteroid Orbits," *Icarus* 154: 412-431.

[19] Montenbruck, O. and Gill, E., "Satellite Orbits: Models, Methods, Applications," Springer, 2000.

[20] Rossi, A., "Population Models of Space Debris." In: Milani, A., Knezevic, Z. (eds) Dynamics of Population of Planetary Systems, Proceedings of IAU Coll. 197, 427-438, CUP, 2005.

[21] Rossi, A., "The Earth Orbiting Space Debris," Serb. Astron. J. 170: 1-12, 2005.

[22] Roy, A.E., "Orbital Motion," Institute of Physics, 1988.

[23] Scheeres, D.J., Hsiao, F.Y., Park, R.S., Villac, B.F., and Maruskin, J.M., "Fundamental Limits on Spacecraft Orbit Uncertainty and Distribution Propagation," accepted for publication in the Journal of the Astronautical Sciences, 2007.

[24] P. Seitzer et al. 2004. "MODEST Observations of Space Debris at Geosynchronous Orbit," *Advances in Space Research* 34: 1139-1142.

[25] G. Tommei, A. Milani and A. Rossi. 2007. "Orbit Determination of Space Debris: Admissible Regions," *Celestial Mechanics and Dynamical Astronomy* 97: 289-304.